Narodowe Centrum Badań Jądrowych
National Centre for Nuclear Research
ŚWIERK

# DEVELOPMENT OF LOCALIZED COUPLED NEUTRONIC AND CFD CALCULATION FOR HTR APPLICATION

Michał Górkiewicz

A thesis submitted in fulfillment of the requirements for the degree of Doctor of Physical Sciences in Department of Complex System

Supervisor:
Prof. dr hab. inż. Jerzy Cetnar

Auxiliary supervisor:
Dr inż. Jakub Sierchuła

Otwock 2023

**Acknowledgments**

I would like to thank my supervisor, Professor Jerzy Cetnar, for his scientific supervision, without which this thesis would not have been written.
My thanks also extend to the auxiliary supervisor, Dr. Jakub Sierchuła, for his valuable guidance and support.
I would like to express my gratitude to the leadership of the PhD4GEN project, especially Professor Mariusz Dąbrowski and Dr. Karol Kowal, for creating a friendly environment to work in, as well as providing motivation.
Special thanks to Professor Jaakko Leppänen and Dr. Ville Valtavirta, for their short yet fruitful collaboration which resulted in the interesting concepts used in this thesis.
It is my pleasure to extend my heartfelt thanks to my friends in the PhD4GEN project for the adventure we had together and for supporting each other. I also thank my other friends for their relentless faith in me, especially when I didn't have it myself.
Finally, I sincerely thank my parents, brothers, and family for their support and curiosity, which infused me with a sense of purpose in my work.

# Contents

## Author's Contribution

The present thesis is based on the publication below:
Górkiewicz, M.; Cetnar, J. Flattening of the Power Distribution in the HTGR Core with Structured Control Rods. Energies 2021, 14, 7377. https://doi.org/10.3390/en14217377

# List of Figures

# List of Tables

## Nomenclature

### Greek symbols

| | |
|---|---|
| $\rho$ | density, $[\frac{kg}{m^3}]$ |
| $\kappa$ | thermal conductivity, $[\frac{W}{mK}]$ |
| $\mu$ | dynamic viscosity, $[Pa \cdot s]$ |
| $\omega$ | specific dissipation rate, $[\frac{1}{s}]$ |

### Latin

| | |
|---|---|
| $O$ | distribution parameter, [-] |
| $P$ | power density, $[\frac{W}{m^3})]$ |
| $p$ | pressure, [Pa] |
| $h$ | height, [m] |
| $r$ | radius, [m] |
| $C_p$ | specific heat, $[\frac{J}{kg \cdot K}]$ |
| $\dot{m}$ | mass flow rate $[\frac{kg}{s}]$ |
| $U$ | velocity $[\frac{m}{s}]$ |
| $k$ | turbulence kintetic energy $[\frac{m^2}{s^2}]$ |
| $I$ | turbulence intensity [-] |
| $l$ | turbulence lenght scale [m] |

### Subscripts

| | |
|---|---|
| i | referring to i-th element |
| axial | referring to axial direction |
| radial | referring to radial direction |
| PC | referring to porous carbon |
| PyC | referring to pyrolityc carbon |
| C | referring to graphite |
| He | referring to helium |
| void | referring to fuel pellet inner hole |
| fuel | referring to fuel pellet |
| gap | referring to thermal resistance layer |
| sleeve | referring to graphite sleeve border |
| coolant | referring to coolant hole |

## Acronyms

**AGH UST** Akademia Górniczo-Hutnicza

**AVR** Arbeitsgemeinschaft Versuchsreaktor

**BP** Burnable Poison

**CFD** Computational Fluid Dynamics

**CSG** Constructive Solid Geometry

**DOM** Discrit Ordinance Method

**FSV** Fort Saint Vrain

**HTGR** High Temperature Gas-Cooled Reactor

**HTR-PM** High-Temperature Gas-Cooled Pebble-bed Module

**HTTR** High Temperature engineering Test Reactor

**INET** Institute of Nuclear Technology

**IPyC** Inner Pyrolityc Carbon

**JAEA** Japan Atomic Energy Agency

**JAERI** Japan Atomic Energy Research Institute

**KERMA** Kinetic Energy Released per MAss unit

**MA** Minor Actinides

**MCB** Monte Carlo Continuous Energy Burnup

**MCNP** Monte Carlo N-Particle Transport Code

**NIST** National Institute of Standards and Technology

**OPyC** Outer Pyrolityc Carbon

**RANS** Reynolds Averaged Navier-Stokes

**SiC** Silicone Carbide

**SIMPLE** Semi-Implicit Method for Pressure Linked Equation

**THTR** Thorium High-Temperature Reactor

**TRISO** TRistructural-ISOtropic

**Abstract**

High-Temperature Gas-Cooled Reactors (HTGRs) are promising for multiple applications, including power generation, water desalination, the chemical industry, or hydrogen production. Existing safety standards in the nuclear industry require that reactor safety be maintained under all conditions.

In high-temperature reactors, the temperature of the fuel, in the form of TRI-structural ISO-tropic (TRISO) capsules is an important issue, as overheating them can risk the release of radioactive fission products from the fuel. On the other hand, these reactors have inherent safety features due to the negative temperature coefficient. This coefficient consists of phenomena that cause power to decrease with fuel temperature growth, such as the temperature Doppler effect and hardening of the neutron energy spectrum. To consider these phenomena, it is necessary to carry out coupled thermal-fluid and neutronic calculations.

A significant challenge in modeling high-temperature reactors is their complex structure, which consists of fuel elements with TRISO particles. While accounting for this dual heterogeneity is not a challenge in neutronic calculations, it is very difficult in thermal-fluid calculations, even using Computational Fluid Dynamics (CFD) calculations. It should also be noted that the aforementioned CFDs, due to their high requirements, are not suitable for modeling the entire reactor, but can be effectively used for more accurate calculations of a smaller component, such as a fuel rod.

This thesis presents the characteristics of high-temperature gas-cooled reactors, their history, and the phenomena affecting the temperature coefficient. An example of integrated calculations, which was the PUMA project using MCB and POKE software, is also presented. To demonstrate the relevance of the relationship between power distribution and temperature distribution, simulations of reactor operations with an innovative control rod structure were carried out. The result was a significant equalization of power distribution and a reduction of temperatures in the core. The purpose of this work was to demonstrate that accurate CFD calculations can support integrated thermal-fluid and neutronic calculations by more accurately representing the smaller reactor component.

A single fuel rod model in OpenFOAM was run for the previously presented calculations in MCB and POKE to more accurately represent the local temperature distribution. Temperatures lower than in POKE were obtained, nevertheless with a simplification of the homogeneous heat distribution. To verify this simplification, the Serpent program was used, providing the ability to perform integrated calculations with OpenFOAM using the multi-physics interface and the ability to work on a random TRISO distribution. These calculations resulted in temperatures higher

by only about 10 K, which can be regarded as a margin of error during normal reactor operation. However, the studies should be continued in order to determine the meaning of other factors connected with the properties of the mesh or TRISO particles and to allocate the methodology to a full core model.

**Streszczenie**

Reaktory Wysokotemperature Chłodzone Gazem (HTGR) są obecnie obiecującą technologią do wielorakich zastosowań, wliczając w to produkcję energii, odsalanie wody, przemysł chemiczny czy produkcję wodoru. Obowiązujące w przemyśle jądrowym standardy bezpieczeństwa wymagają, aby w każdych warunkach zachować bezpieczeństwo reaktora.

W reaktorach wysokotemperaturowych istotną sprawą jest temperatura kapsułek TRISO, gdyż przegrzanie ich może grozić uwolnieniem radioaktywnych produktów rozszczepienia z paliwa. Z drugiej strony, reaktory te charakteryzują się inherentnymi cechami bezpieczeństwa wynikającymi z ujemnego współczynnika temperaturowego. Na ten współczynnik składają się zjawiska powodujące zmniejszanie mocy ze wzrostem temperatury paliwa, takie jak temperaturowy efekt Dopplera czy utwardzenie spektrum energii neutronów. Do uwzględnienia niniejszych zjawisk konieczne jest przeprowadzenie zintergrowanych obliczeń cieplno-przepływowych i neutronicznych.

Znaczącym wyzwaniem w modelowaniu reaktorów wysokotemperaturowych jest ich złożona struktura, na którą składają się elementy paliwowe z cząstkami TRISO. O ile uwzględnienie tej podwójnej heterogeniczności nie stanowi wyzwania w obliczeniach neutronicznych, to jest bardzo trudne w obliczeniach cieplno-przepływowych, nawet z wykorzystaniem numerycznej mechaniki płynów (CFD). Należy również zauważyć, że wspomniane CFD z racji na swoje wysokie wymagania nie są odpowiednie do modelowania całego reaktora, ale mogą być skutecznie wykorzystane do dokładniejszych obliczeń mniejszego elementu, takiego jak pręt paliwowy.

W niniejszej pracy przedstawiono charakterystykę reaktorów wysokotemperaturowych chłodzonych gazem wraz z ich historią oraz zjawiskami mającymi wpływ na współczynnik temperaturowy. Przedstawiono też przykład zintegrowanych obliczeń, jakim był projekt PUMA, wykorzystujący programi MCB oraz POKE. Dla pokazania istotności związku z między rozkładem mocy a rozkładem temperatury przeprowadzono symulacje operacji reaktora z innowacyjną strukturą prętów kontrolnych. Efektem było znaczące wyrównanie rozkładu mocy i zmniejszenie temperatur w rdzeniu. Celem niniejszej pracy było wykazanie, że dokładne obliczenia CFD mogą wspierać zintegrowane obliczenia cieplno-przepływowe i neutroniczne poprzez dokładniejsze odwzorowanie mniejszej składowej reaktora.

Do przedstawionych wcześniej obliczeń w MCB i POKE wykonano model pojedynczego pręta paliwowego w OpenFOAM, którego zadaniem było dokładniejsze odwzorowanie lokalnego rozkładu temperatury. Uzyskano temperatury mniejsze niż w POKE, niemniej przy uproszczeniu jednorodnego rozkładu ciepła. Aby zwery-

fikować to uproszczenie wykorzystano program Serpent, dający możliwość przeprowadzenia zintegrowanych obliczeń z OpenFOAM z wykorzystaniem specjalnego interfejsu oraz możliwości pracy na losowym rozkładzie TRISO. W wyniku tych obliczeń uzyskano temperatury większe jedynie o ok. 10 K, co można traktować jako margines błędu podczas normalnej operacji reaktora w analizowanym przypadku. Wymagane jest jednak przeprowadzenie dalszych badań celem zidentyfikowania roli czynników związanych z siatką czy właściwościami TRISO, a także uwzględnienie przedstawionej metodologii w obliczeniach całego rdzenia.

# 1 Introduction

High Temperature Gas-Cooled Reactor (HTGR) can be used for various co-generation industrial applications. Among them the GEMINI initiative working on nuclear cogeneration[17] or the development of hydrogen production technology applying HTGR performed by Japan Atomic Energy Agency (JAEA) [42]. There have been decades of experience with this technology that has proven its safety and reliability [35]. One example is the High Temperature engineering Test Reactor (HTTR) in Japan, which served several safety experiments, including continuous work at a reactor output coolant temperature of 950°C[42]. One of the most significant components of HTGRs is their fuel in the form of TRistructural-ISOtropic (TRISO) particles, which can contain confined fission products at very high temperatures (above 1600°C)[1]. Hence, it is essential for reactor safety performance analysis to predict and accurately calculate the temperature distribution in the core in order to assess and reduce the risk of TRISO particle failure. To do this, one should consider not only the thermal-hydraulic properties of the core, but also neutronic properties due to existing feedback between the temperature and the power. This can be achieved by performing coupled neutronic and thermal-hydraulic calculations [16, 47, 29]. An example of the coupled calculation is the MCB - neutronic burnup code[4], internally coupled with the POKE, system thermal-hydraulic code system [38], designed specifically for prismatic HTGR cores. Those codes proved their applicability for full-core reactor analysis, however, simulations of accidents or local coolant flow disturbance are beyond the applicability of the POKE. The Computational Fluid Dynamics (CFD) codes can cover a wide range of thermal-hydraulic phenomena, but at a high computational cost. This makes them unpractical for full core analysis[44] unless far simplifications are being done (for example porous media models combining solids and fluids into one medium and introducing porosity coefficient into fluid transport equations) [13]. Henceforth, the CFD analysis could be performed locally, i.e for a part of the analyzed core (single fuel block, column, rod, etc.), to support full-core models. A coupling of CFD and neutronic codes has also been done, which is the case of the Serpent neutronic code and the OpenFoam CFD [47, 32, 30].
In the thesis, the neutronic and thermal-hydraulic properties of HTGRs will be discussed, as well as phenomena responsible for power and temperature feedback. The above codes will be described followed by a description of the basics of Monte Carlo methods used by Monte Carlo Continuous Energy Burnup (MCB) and Serpent codes, and the basics of CFD used by the OpenFoam. The development of neutronic and CFD models of an HTGR fuel rod will be presented as well as the coupling methodology. Simulations of an entire reactor core in MCB and POKE will

be performed with additional OpenFoam localized calculations. Then, the power discretization will be investigated in simulations using the same OpenFoam model and an analogical model in the Serpent code, with application of the Serpent multi-physics interface.

## 1.1 Motivation

HTGR cores are characterized by significantly different neutronic and thermal-hydraulic properties compared to other systems like Light Water Reactors or Fast Breeding Reactors. Due to the long neutron migration length in graphite, long-range neutronic spatial effects should be taken into consideration. Yet, deep neutron thermalization imposes high flux gradients and other important effects. The double heterogeneity of the reactor core caused by a fine structure of fuel compacts containing TRISO fuel particles also should be taken into consideration for assessing the neutron spectra effects. Those features can be significant for the thermal-hydraulic performance of the reactor due to existing feedback between core temperature and power distributions. The feedback is caused by the Doppler broadening effect and the fact that the energy of the thermalized neutron is the thermal equilibrium energy of the core, which obviously depends on the core temperature. Due to declared TRISO particles properties, such as high resistance to their damage, it is essential to identify and assess physical conditions that can cause release of radioactive material from the fuel.

## 1.2 Objective of the thesis

The research goal of the thesis is the examination of the possibility of coupling neutronic and localized CFD calculations for prismatic HTGR core. Localization of CFD calculation is to consider a part of the core (block, column, rod, etc.), taking the boundary and initial conditions from the model of the full core.

## 1.3 Research hypothesis

Coupled neutronic and localized CFD calculations in OpenFoam can supplement full core performance analyses in MCB and POKE with increased resolutions in locations of possible hot spots, where necessary, possibly enabling the simulation of the coolant flow disturbance. Yet, this approach can offer a good compromise between resolution of calculated results around important locations in affordable and computational requirements of CFD calculations.

## 1.4 Outline

The structute of the thesis is as follows:
In section 2 a general characterization of HTGRs is provided with regard to its design, history, thermal-hydraulic and neutronic properties, and occuring temperature feedback.
In section 3 an example of coupled thermal-hydraulic and neutronic calculation on HTGRs are presented with regard to the applied coupling schemes and methods.
In section 4 the Monte Carlo for neutronic calculations is briefly explained as well as the MCB code, and the neutronic model of a HTGR reactor in the MCB is described.
In section 5 the CFD method for thermal-hydraulic calculations is briefly explained and the conjugated heat transfer model for HTTR fuel column in OpenFoam is described in detail. The description of the model contains necessary informations regarding the applied solver, geometry and mesh, applied material propeties and boundary condition.
In section 6 the Serpent code is briefly described with its multi-physics interface, and the HTTR fuel rod model is described.
In section 7 the results are discussed and the work is concluded.

# 2 Review of High-Temperature Gas-Cooled Reactors (HTGRs)

The key characteristics of HTGRs are the fully ceramic fuel in the form of TRISO particles, graphite moderator, gaseous coolant, and high reactor outlet temperature (typically between 750°C and 950°C)[20]. HTGRs possess inherent safety features and superior fission product retention within the fuel and graphite in comparison to conventional reactor technology [18].

TRISO-coated particles consist of a dense spherical heavy metal kernel of heavy metal oxides, carbides, or a mixture of both. The fuel kernel is surrounded by four coating layers: a porous pyrocarbon buffer layer, a highly isotropic Inner Pyrolityc Carbon (IPyC), a Silicone Carbide (SiC) layer, and an Outer Pyrolityc Carbon (OPyC). The coating layer of the TRISO fuel particles inhibits fission product release and migration from the fuel. Typical TRISO-coated particles have an overall diameter in the range of 500-1000 m[28]. The TRISO particles distribution in HTGRs cores is shown in fig. 1

There are two general types of HTGRs cores - prismatic and pebble bed. The prismatic core type is a grid of hexagonal fuel blocks. The blocks are stacked on top of each other to form a prismatic shape and coolant flows through channels between the blocks. Fuel blocks typically consist of a graphite matrix with TRISO fuel particles dispersed therein. The prismatic core design is modular, allowing for easy replacement of individual fuel blocks for easy maintenance and refueling. The pebble bed core type uses fuel particles packed into graphite spheres the size of a tennis ball and placed in a cylindrical vessel. Coolant flows through the gaps between the spheres, transferring heat from the fuel particles to the further energy conversion system.

Due to high outlet reactor temperature, HTGRs have a wide range of potential applications for industrial processes. Among them, one can mention: district heating, seawater desalination, pulp and paper production, oil recovery from oil sands, oil recovery from oil shale, oil refining, chemicals production, soda ash production via Solvay process, aluminium production, ammonia production, hydrogen production, lime, and iron and steel making [20].

## 2.1 Background and development of HTGRs

A high-temperature, gas-cooled, graphite-moderated reactor is one of the first projects to use nuclear fission for civilian purposes. As early as 1947, a helium-cooled nuclear reactor project was designed in the United States, fuelled with uranium dispersed in beryllium oxide or graphite pebbles. In the early 1950s, Britain de-

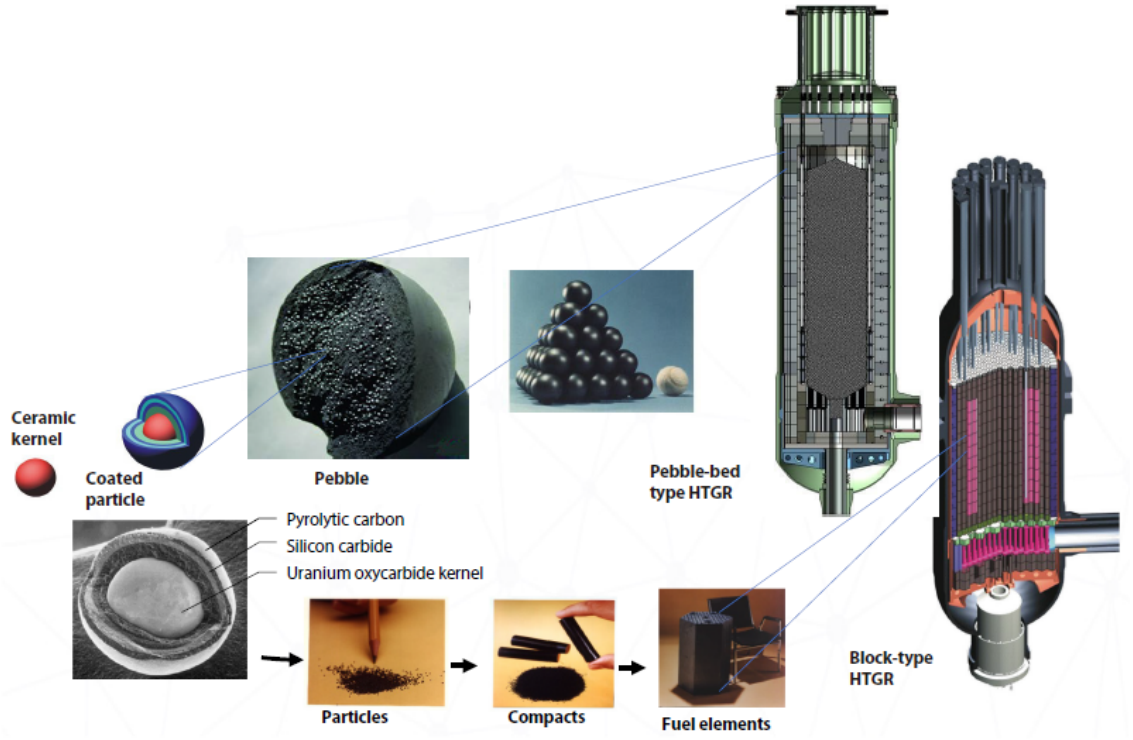


Figure 1: TRISO-coated fuel for pebble-bed type and block-type HTGRs
source: Gougar, H.D., "High Temperature Gas-cooled Reactor – History, Physics, Design Features", Idaho National Laboratory, INL/MIS-19-52882, 2019

veloped the Magnox 11 power reactor, which used natural uranium metal cooled with carbon dioxide. The first of four Magnox reactors built at Calderhall, England, was connected to the grid in August 1956 (60 MW electrical output). A notable feature of the Magnox reactor is that it would have been safe, of course, if the CO2 inventory had been maintained, even in the event of an unprotected loss of coolant. The Dragon reactor in the UK was the first high-temperature helium-cooled reactor to reach criticality (1966). The Peach Bottom HTR, developed by General Atomics, reached criticality in May 1967. Because it used helium, an inert gas, Peachbottom tolerated temperatures at least twice as high as in the Magnox reactor. During the same period, Germany used technology invented in the United States in the 1940s to develop a design pebble-bed core. The result was the experimental Arbeitsgemeinschaft Versuchsreaktor (AVR). It was connected to the grid in December 1967. The AVR experienced several safety incidents during its operation, including a fuel pebble failure in 1978 and a coolant leak in 1986. Despite this, higher-capacity industrial models were designed. Namely, the Fort Saint Vrain (FSV) power plant in Colorado (USA) and Thorium High-Temperature Reactor (THTR) in North Rhine-Westphalia, Germany. The Fort Saint Vrain reactor originally had a power capacity of 330 MW. Its core was coated with graphite rods

(compacts) and consisted of fuel in the form of spherical particles contained inside, which were embedded in prismatic graphite blocks. The THTR had a power capacity of 300 MW and a pebble core. The power shift from 15 MW (AVR) to 300 MW was achieved by increasing the core diameter and power density. The Fort Saint Vrain reactor was connected to the grid in 1976. After 13 years of operation, it was closed in 1989 due to the prohibitive cost of incrementally upgrading prototypes and fixing design flaws. THTR operated for only four years after its 14-year construction period (1971-1985), which featured tightening safety requirements after the Three Mile Island accident. The THTR also suffered from various technical issues that greatly reduced its lifespan. Several safety problems occurred during the THTR's operation, including a ruptured fuel grid in 1986 and a coolant leak in 1988. These incidents contributed to the decision to shut down the reactor in 1989 [35, 40].

Currently operating HTGRs are Japanese HTTR with prismatic core and Chinese HTR-10 and High-Temperature Gas-Cooled Pebble-bed Module (HTR-PM) with pebble bed cores.

The main purpose of HTTR is to build and extend the technological base of an advanced HTGR and conduct various irradiation experiments for innovative high-temperature fundamental research. Construction was completed in May 1996. Fuel loading began on July 1, 1998, from the core peripherals. The first criticality was achieved on November 10, 1998, with a 19-row annular core. The first full load operation was completed on December 7, 2001, with an average core exit temperature of 850 °C, and the HTTR operating license was granted on March 6, 2002. The reactor exit coolant temperature was 950°C at the maximum power of 30 MW. It was achieved for the first time in the world on April 19, 2004. From January to March 2010, the HTTR worked normally under high temperatures and full load conditions for 50 days [14, 24]. The reactor was shut down after the Fukushima accident in 2011, but its operation was resumed on July 30,2021 [25]. The research using HTTR is conducted in terms of confirmation of inherent safety of HTGRs, and hydrogen production[26].

The HTR-10 is China's first major step in modular HTGR development. Planned as part of China's High-Tech Research and Development Program, it was approved by the State Council in March 1992 and built on the site belonging to the Institute of Nuclear Technology (INET) of Tsinghua University. The INET is responsible for the overall design, construction and operation of this test reactor. Construction of the facility was completed in 2000 and the first criticality occurred in December 2000. The HTR-10 Design Criteria and Safety Analysis Report were approved in August 1992 and March 1993, respectively. A basic design and budget estimate were

completed and subsequently approved by the National Education Commission and the National Science and Technology Commission in 1994[14].
The HTR-PM is a demonstration nuclear power plant owned by a consortium led by China Huaneng, China Nuclear Engineering Corporation, and INET. The construction started in 2012. The HTR-PM consists of two pebble-bed HTGRs (each of 250 MWt) connected to a single 210 MWe steam turbine. The first criticality was reached in September 2021, and the initial full power in December 2022 [49, 50].

## 2.2 Thermal-hydraulic properties

Graphite is a carbon allotrope composed of a series of hexagonal network carbon atoms as shown in Figure 2. The layered structure of graphite results in strong anisotropic properties, such as thermal expansion and thermal conductivity. Nevertheless, because of their extremely high thermal conductivities, graphite and its composites are considered to be the most promising thermal management materials [36]. Helium as an inert gas does not cause materials corrosion, even at high

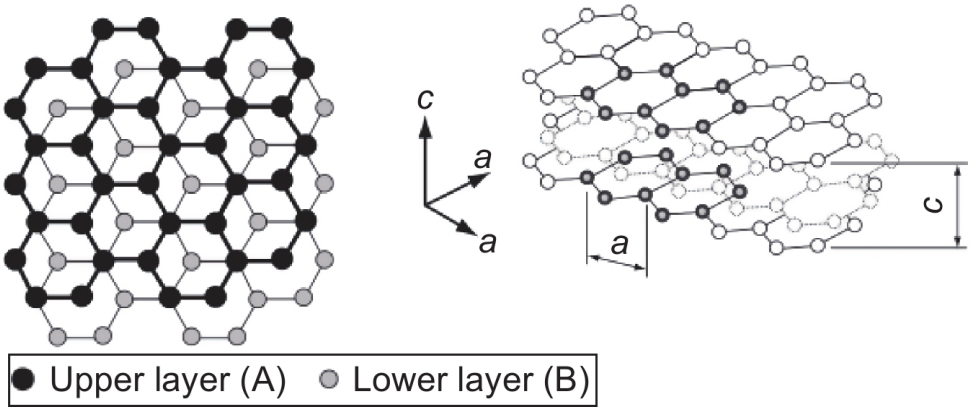


Figure 2: Schematic diagram of graphite structure. [36]

temperatures. Moreover, it is not subject to phase transformations in any reactor working conditions, assuring a single-phase flow. Due to its small viscosity, it can flow through small coolant channels or spaces between graphite pebbles.

## 2.3 Neutronic properties

The process of moderation is decreasing the energy of neutrons as they collide with the nuclei of the moderator. The probability of fission, known as fission cross-section, grows as the energy of neutron decreases [15]. Figure 3 shows the fission cross-section for U-235 as a function of an incident neutron energy, from which one can see that for sufficiently low energies, the cross-section is inversely proportional

to the neutron energy. Thus, moderation essentially increases the effectiveness of the fission chain reaction. Neutrons whose energy is equal to the thermal equilibrium energy of the medium are thermalized. The most common moderator used in the nuclear industry is water, but more specifically, hydrogen atoms contained in water. Graphite used in HTGRs can differ significantly as moderators. With each collision, neutrons transfer a part of their energy to the collided nucleus. The amount of the transferred energy depends on the mass of the moderator's nuclei. The lower the mass, the more efficient the moderation, thus hydrogen would be the most efficient moderator. On the other side, one should take into account the neutron absorption of a moderator, and taking that into account, deuterium can be considered an even more efficient moderator. Graphite used in HTGRs has higher mass, thus poorer moderating properties[33]. As a consequence, many (above 100) collisions are required to thermalize a neutron. Nevertheless, due to the high moderator-to-fuel volume ratio, HTGRs are characterized by deep neutron thermalization, which means that a high fraction of neutrons in the core is thermalized. This imposes a short distance that a neutron can travel in the reactor, and as a consequence high flux gradient, especially in the vicinity of control rods and reflectors. Another specific feature of HTGRs is double heterogeneity caused by a fine structure of the fuel, causing relatively low average power density [5].
In LWRs moderator serves as a coolant at the same time. This is not the case for HTGRs, as helium has far too small density to act a significant role in the process of moderation, even though it possesses decent other moderation properties [33].

## 2.4 Temperature feedback

As it was discussed in the previous paragraph, the behavior of a reactor highly depends on numerous cross-sections of the fuel and the moderator. Moreover, the cross-section highly depends on neutron energy. In fact, the actual dependence is on the relative speed between the neutron and the nucleus [34]. Thus, the random thermal motion of a medium should be taken into consideration for phenomena occurring in a reactor. Moreover, as it was mentioned, thermalization occurs when a neutron reaches the energy of the thermal equilibrium. It means that the higher temperature, the higher the equilibrium energy of neutrons, and in a consequence, the lower the probability of fission. This is also known as the hardening of the neutron spectrum. Another important phenomenon is the Doppler broadening of resonance capture cross-section, which is the probability of capturing a neutron of intermediate energy (i.e. during the moderation process). This effect is caused by the fact that as the temperature of the fuel rises, so does the thermal vibration of

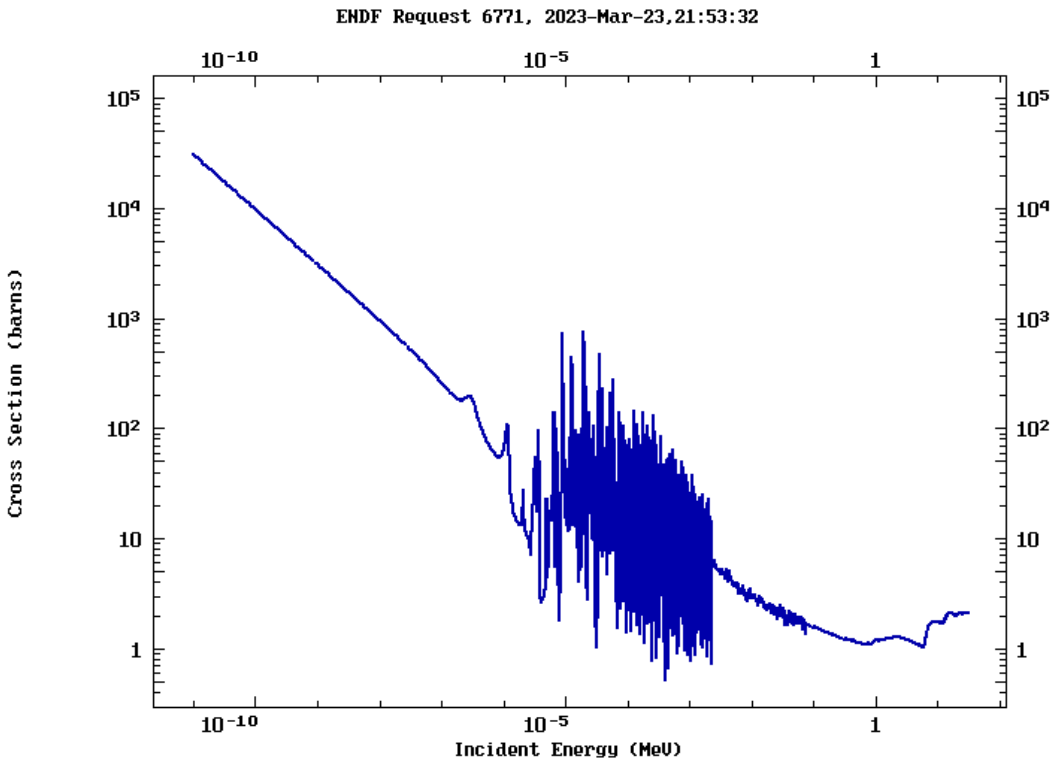


Figure 3: Fission cross-section of U235.
source:[15]

the fuel nuclei. As a result, the range of neutron energies that correspond to the increased thermal vibration of the fuel nuclei expands, as do the resonance peaks in the absorption cross-sections of the fuel nuclei [10]. It is especially significant in the case of graphite-moderated reactors since a high number of neutron collisions increases the time of exposition of the neutron to the resonance capture. It is worth mentioning that thermal expansion has a significant effect on liquid-moderated reactors, like light water reactors, due to the increase in the distance that neutron travels between collisions. This effect is essential in the case of boiling water reactors, as the moderator density rapidly decreases during the boiling process [11]. Nevertheless, this phenomenon is far less important in the case of graphite-moderated reactors due to the small thermal expansion coefficient of graphite. Moreover, differently compared to light water reactors, the thermal expansion of the helium coolant does not play any other significant role other than transporting heat from the graphite core structure.

# 3 Coupled Thermal-hydraulic and neutronic calculations of HTGRs

High operating temperatures of HTGRs require high-temperature resistant materials in order to prevent a release of the radioactivity of fission products and to ensure the endurance of a reactor structure. Thus, the assessment of temperature distribution and its maxima is an essential part of research conducted on HTGRs. Specific features of both prismatic and pebble-bed cores impose challenges in their thermal-hydraulic modeling. This is especially addressed toward cross and by-pass flow in prismatic cores, as well as irregularities of pebble-bed cores. This chapter's discussion will focus mainly on prismatic cores since the work done in the thesis was devoted to a prismatic core. Graphite blocks are vulnerable to shrinking with fast neutron irradiation. This introduces gaps between block columns and layers, and as a consequence, by-pass and cross-flow occur [27]. In order to familiarize the reader with coupled calculations for HTGR, this chapter presents example calculations using coupled MCB and POKE calculations for the PUMA project. These codes will be used later in the work.

## 3.1 PUMA project

The Monte-Carlo Continuous Energy Burn-up (MCB) code is used for calculating a nuclide density evolution with time. It internally integrates the MCNP and Transmutation Trajectory Analysis. The code concerns all possible nuclides that can emerge in the system, and there is no predefined list required, as long as all transmutation chains are being formed automatically online. In reality, the change of nuclide composition evolution in a reactor core can be described as a continuous function of time. MCB approximates that function by the time step procedure. Other features of the code are two sources of decay scheme, the possibility to load numerous cross-section data, and coupling with POKE for prismatic HTR thermal-hydraulics. Reaction rates are calculated by continuous energy method, fission product yield from incident energy-dependent distributions of fission products, and heating by using KERMA factors. It is also possible to simulate the fuel shuffling or CR operations using material processing with material allocation to geometry cells during burn-up. In order to calculate the time evolution, an extended linear chain method based on the Bateman approach is used. Coupling was made in the level of source code, but all the data exchanged between codes are saved in external files, in order to allow the user to recalculate. Reactor geometry and thermal-hydraulics specifications are loaded from the POKE input, while MCB delivers only power distribution.

Nevertheless, the initial temperature profile has to be defined by the user. Then the POKE calculates the required parameters and new temperature profile. Then cross-sections are adjusted to the new temperature and are used for new power distribution iteration, and burnup calculation provides more realistic results. The law of large numbers is assumed in statistical fluctuation in Monte Carlo modeling, so standard formulations of statistical measures of probability are used. However, HTR is one of the nuclear systems which contains a systematic term in fluctuations of power distribution, which is propagated in consecutive neutron generations. The term tends to conserve itself or increase oscillations since the neutron heating rate is used in the process of source normalization to the constrained power, and the process is linked with the production and depletion of 135Xe in a deeply moderated HTR core, but only numerical oscillations instead of physical (which can also occur). When the fundamental distribution of the source is difficult to achieve, another source of oscillations occurs due to the neutron source convergence problem. Both effects can be reduced by the improvement of the source normalization procedure. The procedure is shown in Figure 4, where BOS means Beginning of Step and EOS is End of Step, and it all is called the bridge scheme of burnup.

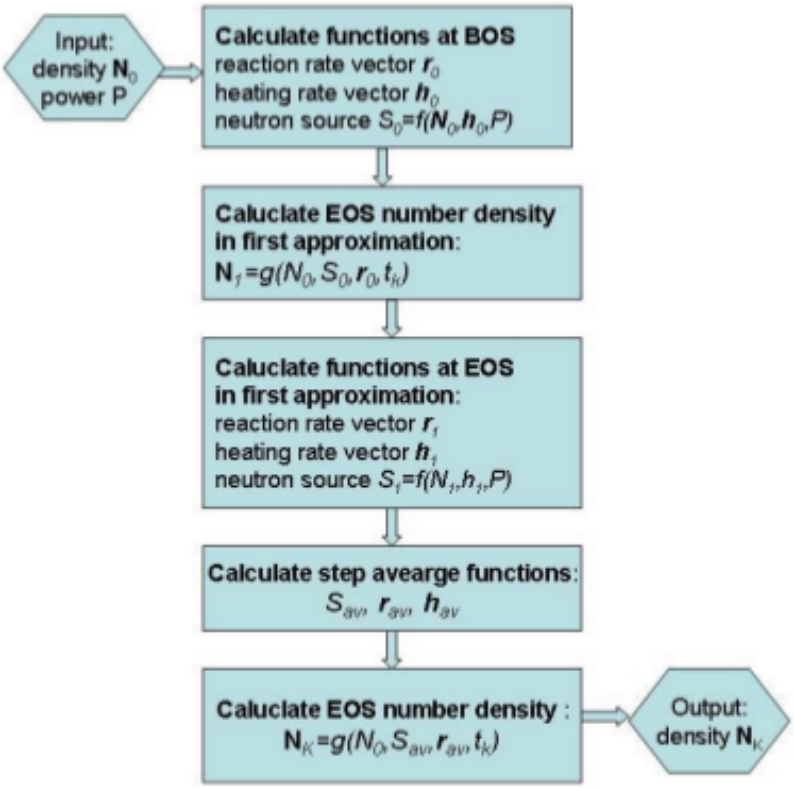


Figure 4: Diagram of bridge scheme for burnup step [5].

The model for calculations was prepared with recommended design options con-

cerning only axial fuel shuffling and 4-batch refueling scheme, and features that are difficult to consider in other methods are especially considered, for example, Control Rods operations. The reference PUMA reactor core comprises five radial rows of fuel blocks in eight axial layers. Radially every block is divided into two halves, and axially into three regions, which gives 240 fuel zones. The core was filled with TRISO particles in an 18% volume fraction. However, every fuel block also has its internal structure. The 4-batch axial-only fuel shuffling was simulated due to its simplicity, reduction of space of an operator error, and short time required. The scheme is shown in the Figure 5 CR channels are axially divided separately with insertion level adjustment of 50cm bins. Burnable poison Eu2O3 was added in the inner region of fuel blocks. Two fuel compositions were modeled, first without and second containing minor actinides, and their cycles lengths to 420 and 350 days respectively.

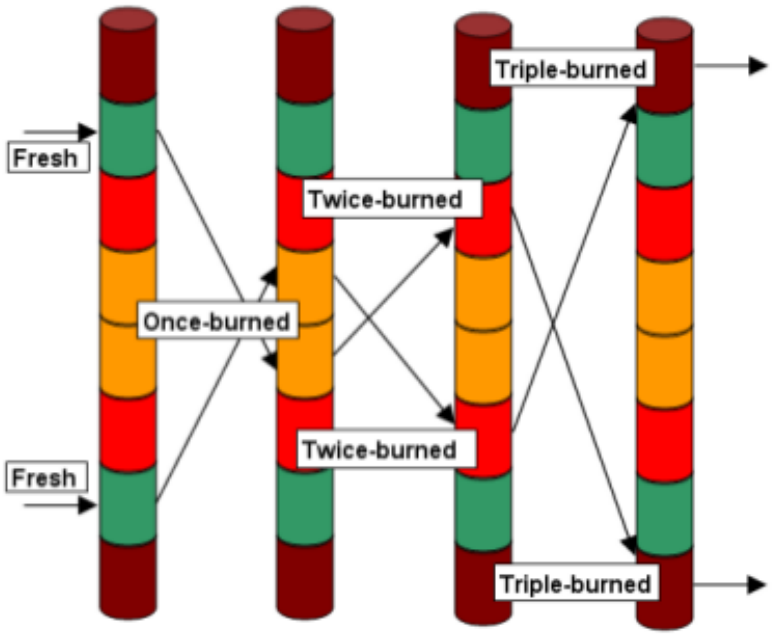


Figure 5: Scheme of 4-batch axial-only block shuffling [5].

The process of transmutations in a deep burn design has significant meaning in that the heavy metal nuclides are able to fission out quickly or create either non-fissile or fissionable nuclides in that process. The consequence of the first case can be the increase of afterheat, nevertheless, the second case can reduce reactivity loss. In this model, the burnup rate can change depending on position even four times, which has a relevant meaning for power distribution. Fission is the main reaction responsible for burnup and heavy metal destruction, thus it terminates the possibility of further transmutation. If a heavy meat avoids fission it can become an active actinide, especially plutonium isotopes, which have a high probability of avoiding fission, and

in consequence, creating non-fissile ones. As it was told earlier, burnup strongly depends on the position, so the same can be seen in the case of branching 238Pu, 241Pu, and 241Am, and  decay as well. In regions with low burnup increased fissile destruction by neutron capture is observed, which leads to a bigger reactivity swing, thus lower achievable burnup. It was determined that, without consideration of burnable poisons and fuel shuffling, the temperature in the vicinity of the reflector achieves an unacceptable level of 1300°C. The Monte-Carlo analyses have shown that fuel that does not contain minor actinides can achieve 1680 full power days of irradiation divided into 4 batches, but when MA is considered, the time reduces to 1400 days. The concentration of 135Xe can have spacial oscillations caused by local tilts of neutron flux, which changes the balance between its production and destruction rates. On the other hand, global chances of neutron flux also affect 135Xe concentration, thus inducing power oscillations. Those oscillations have a collective nature due to their area exceeding block dimensions in the same direction. Usually, the CR operation strongly affects power peaks, especially in PUMA-like systems due to short neutron transport length. Simulations were made for fuel with MA, the CR was inserted 100cm more every 50 days, except for the beginning of the cycle, when 135Xe had to be stabilized. In the beginning, the CR was fully withdrawn, and in the end, fully inserted. The result showed that at the beginning burnable poisons reduce neutron flux in the inner block, thus power distribution is quite well balanced. Nevertheless, lower temperature in the upper region causes greater power generation. Insertion of the CR gave significant changes, causing a power increase in the outer and bottom parts of the core. The power increase in outer blocks is caused by their suppression early in the cycle. What is more, fuel located in the lower part is about 12% deeper burned tan in the upper, and radially the burnup spread is about 22%. Temperature reactivity coefficients were negative in all conditions, and the greatest achievable burnup is 65%.

# 4 MCB/POKE calculations

Providing coupled thermal-hydraulic and neutronic calculations is essential for simulating HTGRs due to the interdependencies and complex interactions between the thermal-hydraulic and neutronic behavior of the reactor. It provides possibility of accurate prediction of temperature distribution, which is crucial for ensuring safe and efficient operation. In order to do it, a power distribution should be calculated. It depends on various factors like fuel burnup and control rod positions. In this chapter, a coupled MCB/POKE calculation is presented, which uses the MCB code to calculate the power profile considering the two factors mentioned earlier, and uses the POKE code to determine the temperature profile. The calculations were performed on the Go_HTR reactor model, and the purpose of the work was to propose a control rod operation strategy to ensure possible flattening of the power profile.

## 4.1 Monte-Carlo method

The Monte Carlo method is a computational technique used in neutronic calculations to simulate the behavior of neutrons within a nuclear system. It is a statistical approach that relies on random sampling and probability distributions to approximate the behavior of the neutrons. The primary goal of neutronic calculations is to simulate the transport of neutrons within a nuclear system. Neutrons can undergo various interactions, including scattering, absorption, and fission. The Monte Carlo method simulates each individual neutron's history by tracking its position, direction, energy, and other relevant properties as it moves through the system. The Monte Carlo method uses random sampling to simulate the behavior of neutrons. At each step of the simulation, various physical quantities, such as the neutron's scattering angle or its interaction type, are sampled randomly from appropriate probability distributions. These distributions are based on known nuclear data, such as cross-section data, which describe the likelihood of specific interactions occurring. The neutron's trajectory is tracked as it moves through the nuclear system. Starting from a known neutron source, the initial position, direction, and energy of the neutron are specified. The neutron's interactions with the surrounding materials are simulated by randomly sampling the appropriate probability distributions. For example, the scattering angle and energy of a neutron after a scattering event are determined through random sampling. At each interaction, the Monte Carlo method determines the type of collision that occurs, such as scattering, absorption, or fission. The probability of each type of collision is based on the corresponding cross-section data. By tracking the number and types of collisions, the method builds statistical

information about the neutron population and their behavior within the system. As the neutrons propagate through the system, various quantities of interest, such as reaction rates or flux distribution, are tallied and accumulated. These tallies provide statistical estimates of the desired parameters. By collecting data from a large number of neutrons, the Monte Carlo method can achieve high precision in its estimates. Once a sufficient number of neutrons have been simulated, statistical analysis is performed on the collected data to calculate the desired quantities. This analysis involves averaging the tallied values, calculating uncertainties, and estimating the confidence intervals for the results. The Monte Carlo method is an iterative process that repeats the particle tracking and statistical analysis steps to refine the results. By increasing the number of simulated neutrons, the precision of the results can be improved. The strength of the Monte Carlo method lies in its ability to handle complex geometries, materials, and interactions. It provides a detailed and accurate representation of neutron behavior within a nuclear system. However, it can be computationally intensive and requires significant computational resources due to the large number of neutrons that need to be simulated to achieve accurate results.

## 4.2 Full core model

The work was performed using the internal coupling of the MCB code with the thermal-hydraulic code POKE [38]. The model is based on the HTGR design, called Go_HTR [6], developed in the Polish national research program on HTR industrial applications as a heat source, and created by the team from the Akademia Górniczo-Hutnicza (AGH UST). The core design used in current studies is based on the fuel rod and block structure designed by the Japan Atomic Energy Research Institute (JAERI) [9], where fuel rods with annular fuel compacts are surrounded by a graphite sleeve and inserted into a cooling channel. The space on the inner side of fuel compact is a gaseous void. Helium is used as the coolant. The detailed structures of fuel rods and TRISO particles are shown in Figure 6. In the model, TRISO particles were arranged in a simple cuboid lattice, as it is shown in Figure 7.

A special feature of the Go_HTR design is the implementation of half-fuel blocks. Those blocks contain CR holes and four rows of fuel compacts instead of seven. They are located in the outermost ring of fuel blocks and serve to make the shape of the active core more cylindrical. Helium is used as the coolant.

Specification of the modeled reactor core is presented in Table 2. Fuel rods were grouped into 240 burnable zones: 10 radial zones according to their radial position,

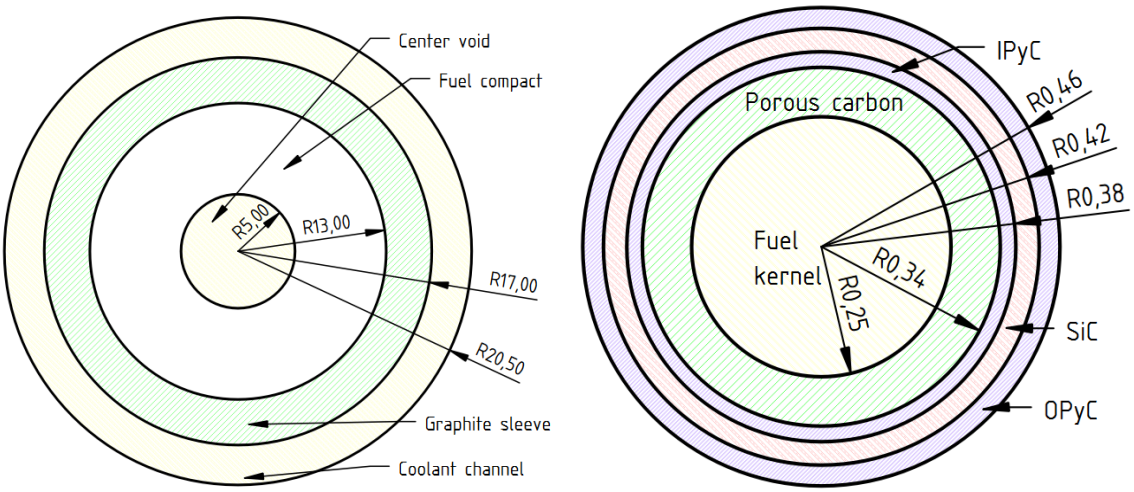


(a) Fuel rod. (b) TRISO particle.

Figure 6: Structure of a fuel rod and TRISO particle. Dimensions are given in mm.

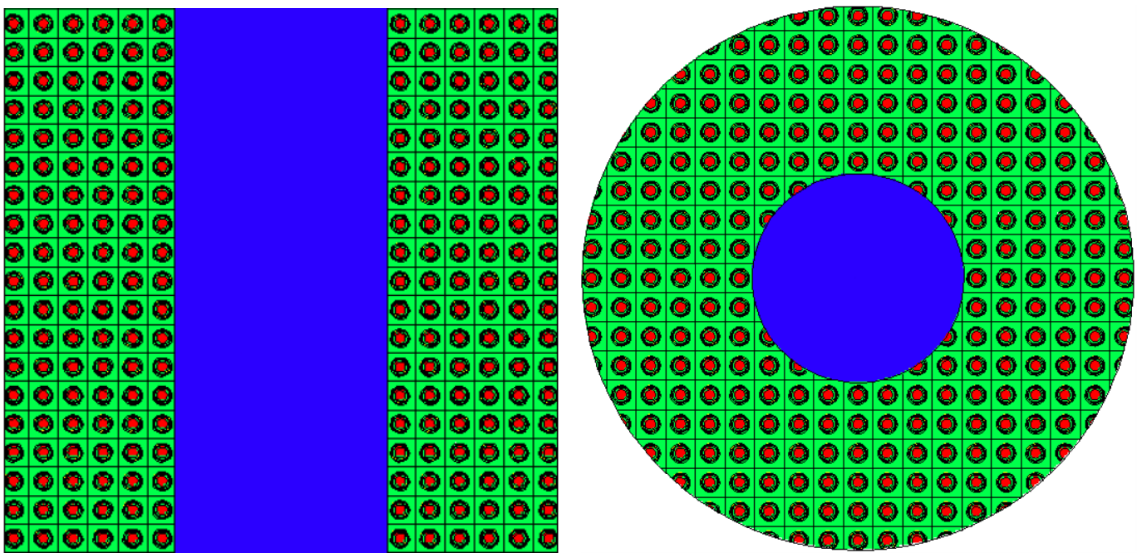

(a) Vertical cross section. (b) Horizontal cross-section

Figure 7: TRISO cuboid lattice arrangement.

each divided into 24 axial zones. Every burnable zone covers one-third of the height of a graphite block. The radial configuration of the reactor core is presented in Figure 8. The letters A, B, C, and D visible in the figure refer to the control rod groups. The control rods have their radial structure divided into just sections: the inner made of B4C in a graphite matrix and the outer made of tungsten. The control rods were grouped into four groups denoted by letters A, B, C, and D. Two groups outside of the active core, A and B, contain six rods each, alternating three in half-fuel blocks and three in moderator blocks. In the active core, two groups, C and D, consist of three alternating control rods each. The numbering of the radial zones starts from the innermost zone 1 (dark yellow rods) and ends with the outermost zone 9 (dark green rods). The exception is a special zone consisting of rods (light yellow) surrounding inner control rods. Purple rings represent control rods, and purple dots represent Burnable Poison (BP). 10000 neutron histories were simulated in 30 inactive and 90 active cycles. The neutron source is distributed uniformly in a cylinder covering the entire active core. Built-in Watt function was used for source neutrons energy distribution. The inlet coolant temperature is 395K, pressure is 4 MPa, and total flow rate is 100 $\frac{kg}{s}$.

Table 2: Specifications of the Go_HTR design [19].

| | **Parameters** | **Values** |
|---|---|---|
| General | Power [MW] | 180 |
| | Fuel enrichment [%] | 12 |
| | Upper/lower reflector thickness [cm] | 120.1 |
| | Core radius [cm] | 200 |
| | Active ore height [cm] | 792.8 |
| | Initial heavy metal mass [kg] | 902.07 |
| | Initial I235 mass [kg] | 108.25 |
| Fuel block | Apothem [cm] | 18.1 |
| | Heigh [cm] | 99.1 |
| | Fuel compacts pitch [cm] | 5.15 |
| | Control rod hole radius [cm] | 5.08 |
| | Graphite density [g $cm^{-3}$] | 1.74 |
| Fuel compact | Height (full compact) [cm] | 93.3 |
| | Height (compact with BP rod) [cm] | 88.4 |
| | Inner radius [cm] | 0.5 |
| | Graphite sleeve inner radius [cm] | 1.3 |
| | Graphite sleeve outer radius [cm] | 1.7 |

**Table 2 continued from previous page**

| Parameters | | | Values |
|---|---|---|---|
| | Radius of the coolant channel hole [cm] | | 2.05 |
| | Packing fraction [%] | | 15 |
| TRISO capsules | Fuel kernel radius [$\mu$m] | | 250 |
| | Fuel kernel density [g $cm^{-3}$] | | 10.65 |
| | Porous carbon outer radius [$\mu$m] | | 345 |
| | Porous carbon density [g $cm^{-3}$] | | 1.05 |
| | IPyC outer radius [$\mu$m] | | 375 |
| | Pyrocarbon density [g $cm^{-3}$] | | 1.9 |
| | SiC outer radius [$\mu$m] | | 420 |
| | SiC density [g $cm^{-3}$] | | 3.18 |
| | OPyC outer radius [$\mu$m] | | 460 |
| Burnable poison | Burnable poison rod radius [cm] | | 0.7 |
| | Burnable poison rod hole radius [cm] | | 0.71 |
| | $Eu_2O_3$ density [g $cm^{-3}$] | | 7.42 |
| | Burnable poison rod heigh [cm] | | 93.3 |
| Control rods | Inner B4C radius [cm] | | 1.97 |
| | Inner tungsten radius [cm] | | 3.8 |
| | Outer radius [cm] | | 4.3 |
| | Lenght [cm] | | 800 |
| | Tungsten isotope mass fraction [%] | W182 | 26.5 |
| | | W183 | 14.3 |
| | | W184 | 30.6 |
| | | W186 | 28.4 |
| | | He4 | 0.2 |
| | Tungsten density [g $cm^{-3}$] | | 19.3 |
| | $B_4C$-graphite matrix density [g $cm^{-3}$] | | 1.31 |
| | $B_4C$-graphite matrix isotope mass fraction [%] | B10 | 3.35 |
| | | B11 | 13.35 |
| | | C12 | 83.3 |

In order to conviniently represent evolution of the power profile, axial and radial power distribution parameters were defined with formulas (1) and (2) respectively:

$$O_{axial} = \frac{\sum_{i=1}^{i_{max}} \overline{p}_{axial,i} h_i}{\overline{p} \sum_{i=1}^{i_{max}} h_i} \tag{1}$$

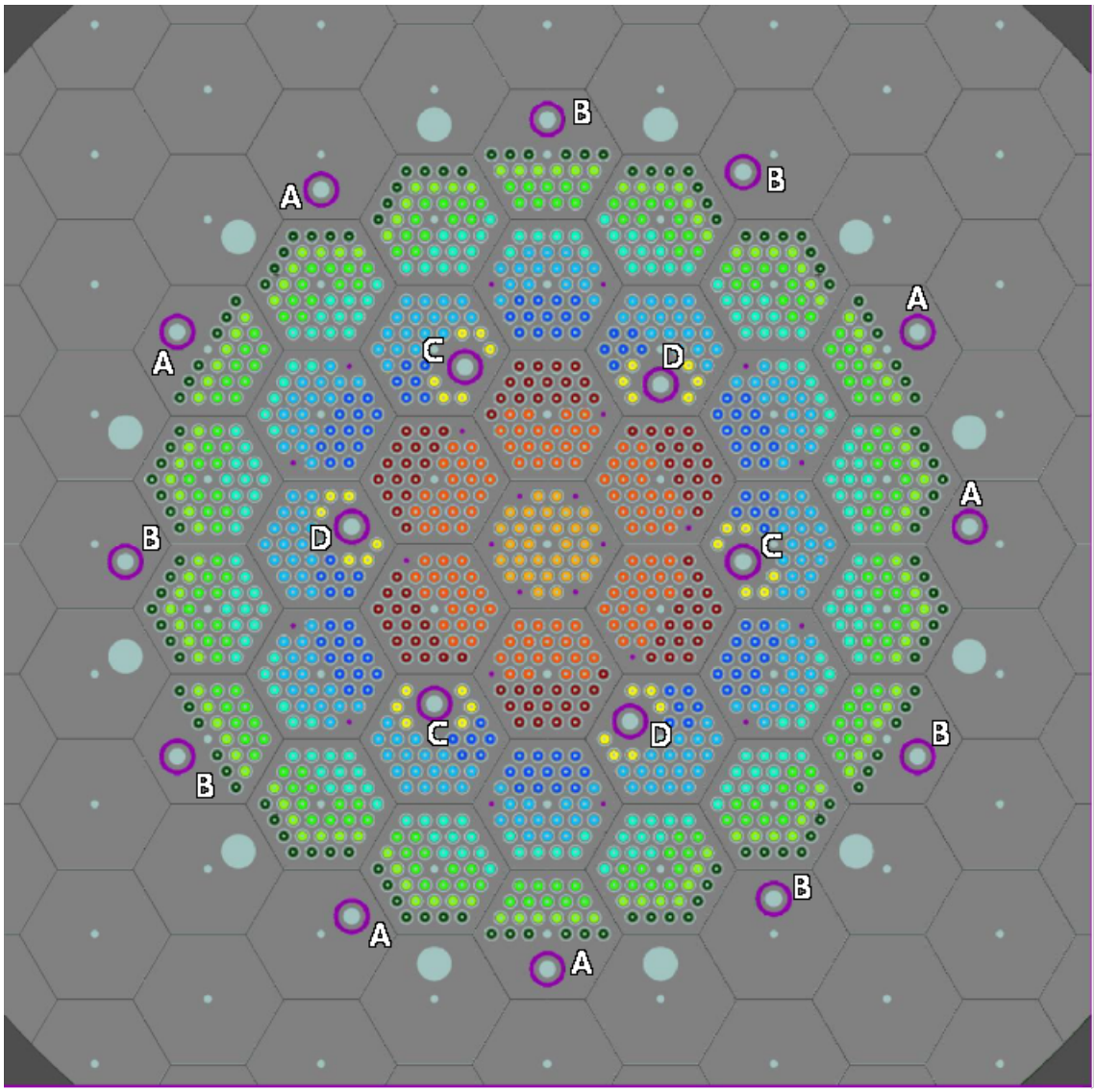


Figure 8: Go_HTR core configuration [19]

$$O_{radial} = \frac{\sum_{i=1}^{i_{max}} \overline{p}_{radial,i} r_i}{\overline{p} \sum_{i=1}^{i_{max}} r_i} \tag{2}$$

Where i refers to burnable zone. The average height of the axial zone is defined as the distance between the top of the core and the axial center of the burnable zone, as shown in Table 3

The positions of the burnable radial zones were assumed as the average distance between the center radial of the core and each fuel rod in the zone and are presented in Table 4. CR refers to the special burnable zone surrounding control rods in the active core. In other words, the axial power distribution parameter is the normalized sum of the power momenta in the burnable zones in the considered direction. The parameter value lower than one means that the power profile is concentrated in the upper half of the core; otherwise, the power profile is concentrated in the bottom

Table 3: Average positions of axial burnable zones.

| $i$ | **1** | **2** | **3** | **4** | **5** | **6** | **7** | **8** |
|---|---|---|---|---|---|---|---|---|
| $h_i(m)$ | 0.1652 | 0.4955 | 0.8258 | 1.1562 | 1.4865 | 1.8168 | 2.1472 | 2.4775 |
| $i$ | **9** | **10** | **11** | **12** | **13** | **14** | **15** | **16** |
| $h_i(m)$ | 2.8078 | 3.1381 | 3.4685 | 3.7988 | 4.1292 | 4.4595 | 4.7898 | 5.1202 |
| $i$ | **17** | **18** | **19** | **20** | **21** | **22** | **23** | **24** |
| $h_i(m)$ | 5.4505 | 5.7808 | 6.1112 | 6.4415 | 6.7718 | 7.1022 | 7.4325 | 7.7628 |

Table 4: Average positions of radial burnable zones.

| $i$ | **1** | **2** | **3** | **CR** | **4** | **5** | **6** | **7** | **8** | **9** |
|---|---|---|---|---|---|---|---|---|---|---|
| $r_i(m)$ | 0.1 | 0.3096 | 0.4496 | 0.5595 | 0.5955 | 0.7134 | 0.8336 | 0.9647 | 1.0316 | 1.0803 |

half of the core. The radial power distribution parameter lower than one means that the power profile is shifted toward the center of the core, whereas higher shows that the power profile is tilted toward the outer region of the core. In the same way, the Xe-135 concentration was analyzed.

Control rod operation was implemented in the calculations in order to observe its impact on the power profile and reactivity evolution. The control rods operation strategy is presented in table 5, and referred further as to St_solid. Moreover, two additional one-day burnup timesteps were implemented in order to reduce xenon numerical oscillations.

The initial power and temperature profiles after the $B_4C$ absorber withdrawal are presented in Figure 9a and Figure 9b respectively. Point 0 in the axial direction is the top of the active core. As one can observe, the power density decreases with distance from the center in the core in the radial direction. It is also the smallest in the top and bottom parts of the reflector. Nevertheless, it does not have a maximum in the axial center of the core due to the application of the burnable poison rods. The radial distribution parameter calculated according to Equation (2), which in this case is 0.92, and the axial parameter is 1.02, which means that the distribution is slightly tilted downward. The temperature also decreases in the radial direction, but increases in the axial direction, from 900 K in the top part of the core to the maximum of 1350 K in the radial center of the bottom part of the core.

The evolution of radial and axial power profiles, as well as profiles of xenon are presented in Figure 10a, and the evolution of power peaking factor and $k_{eff}$ are presented in Figure 10b. One can clearly see the influence of control rod operation on the axial power and xenon profiles, as they fluctuate with the start of operation

Table 5: Specification of St_solid control rod operation strategy.

| **Day, CRs Group** | **3, A** | **8, A** | **15, A** | **25, A** | **35, A** | **45, A** | **55, A** | **65, A** |
|---|---|---|---|---|---|---|---|---|
| **Withdrawn part of CR [%]** | 6.25 | 12.5 | 18.75 | 25 | 31.25 | 37.5 | 43.75 | 50 |
| **Day, CRs Group** | **72, A** | **79, A** | **86, A** | **93, A** | **98, A** | **103, A** | **108, A** | **113, A** |
| **Withdrawn part of CR [%]** | 56.25 | 62.5 | 68.75 | 75 | 81.25 | 87.5 | 93.75 | 100 |
| **Day, CRs Group** | **118, B** | **123, B** | **128, B** | **133, B** | **138, B** | **143, B** | **148, B** | **153, B** |
| **Withdrawn part of CR [%]** | 6.25 | 12.5 | 18.75 | 25 | 31.25 | 37.5 | 43.75 | 50 |
| **Day, CRs Group** | **158, B** | **163, B** | **168, B** | **173, B** | **178, B** | **183, B** | **188, B** | **193, B** |
| **Withdrawn part of CR [%]** | 56.25 | 62.5 | 68.75 | 75 | 81.25 | 87.5 | 93.75 | 100 |
| **Day, CRs Group** | **198, C** | **203, C** | **208, C** | **213, C** | **218, C** | **223, C** | **228, C** | **233, C** |
| **Withdrawn part of CR [%]** | 6.25 | 12.5 | 18.75 | 25 | 31.25 | 37.5 | 43.75 | 50 |
| **Day, CRs Group** | **238, C** | **243, C** | **248, C** | **253, C** | **258, C** | **263, C** | **268, C** | **273, C** |
| **Withdrawn part of CR [%]** | 56.25 | 62.5 | 68.75 | 75 | 81.25 | 87.5 | 93.75 | 100 |
| **Day, CRs Group** | **278, D** | **284, D** | **290, D** | **296, D** | **302, D** | **308, D** | **314, D** | **320, D** |
| **Withdrawn part of CR [%]** | 6.25 | 12.5 | 18.75 | 25 | 31.25 | 37.5 | 43.75 | 50 |
| **Day, CRs Group** | **326 , D** | **332 , D** | **338, D** | **344, D** | **350, D** | **356, D** | **362, D** | **368, D** |
| **Withdrawn part of CR [%]** | 56.25 | 62.5 | 68.75 | 75 | 81.25 | 87.5 | 93.75 | 100 |

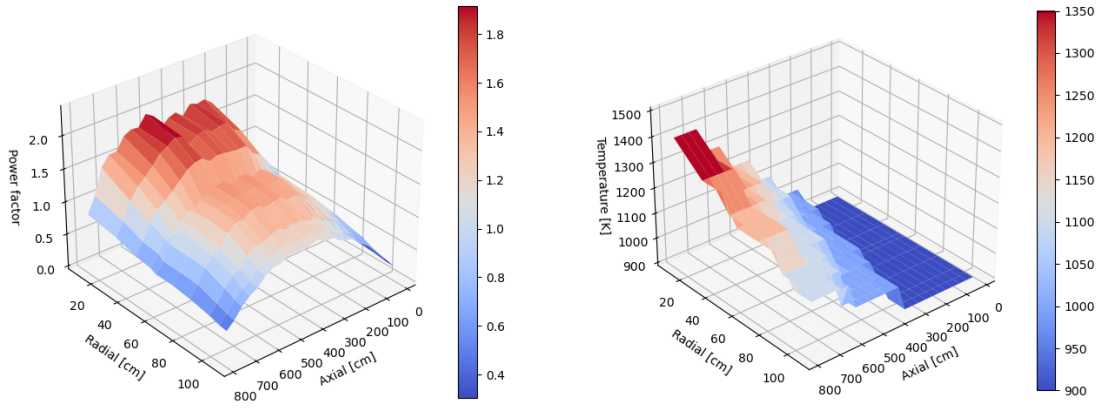


(a) Power distribution.

(b) Temperature distribution

Figure 9: Power and temperature distribution after removal of $B_4C$ from the core.

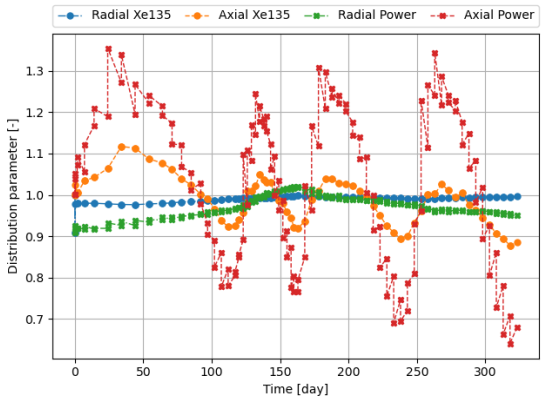


(a) Distribution parameters evolution.

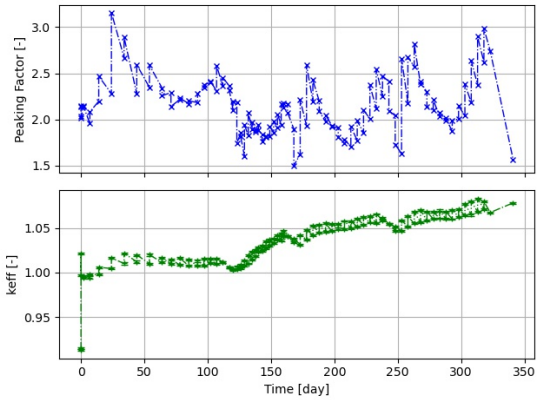


(b) Power peaking factor and $k_{eff}$ evolution

Figure 10: Results of control rod operation strategy St_solid.

of each control rod group. As the control rods are withdrawn, the absorber is removed from the bottom of the core, where the power profile tilts. At the same time, there is an accumulation of xenon, through which the power tilts to the upper part of the core during the last phases of the withdrawal of the control rods. The process is repeated with the start of the operation of the next group of control rods. It can be inferred that the radial power profile flattens as the outer control rods are removed, but later it becomes tilted again toward the core center as the inner control rods are withdrawn. In order to visualize the meaning of the result, power and temperature profiles from day 233 are presented in Figures 11a and 11b. The axial power distribution parameter, in this case, is 0.635, and the radial distribution parameter is 1.02, which confirms that the power is strongly tilted upward the core, but does not significantly change in radial direction. The last is reflected in temperature distribution, as it also does not significantly change in radial direction, but gradually increases in axial direction. One could state that a situation when the temperature is the highest where the power is the lowest, and the opposite, the temperature is the lowest where the power is the highest, is counter-intuitive. This situation is caused by the temperature feedback and proves the necessity of applying coupled thermal-hydraulic and neutronic calculations.

## 4.3 Structured control rods

In order to limit the xenon oscillation caused by the control rod operation, the concept of structured control rods was proposed. The annulus of the control rod was divided into 4 concentric annuli, hereafter referred to as CR layers. The volume shares of each layer were determined by trial and error, and the following division

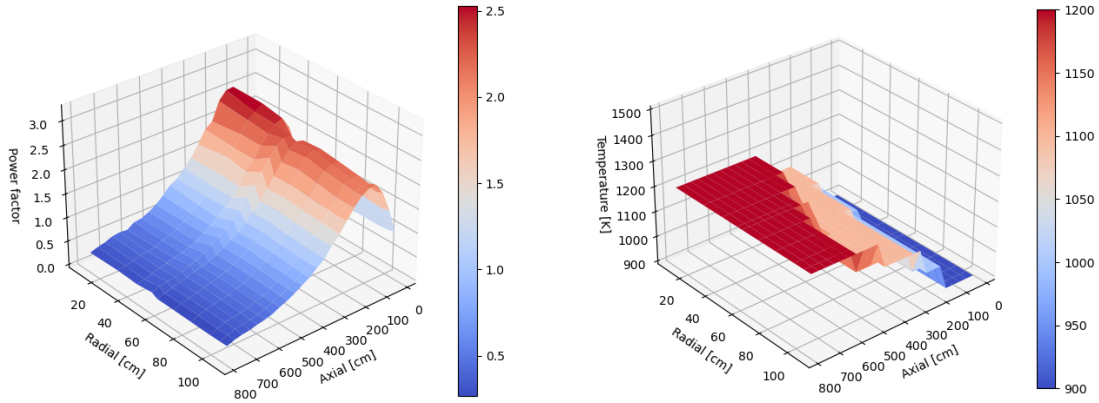


(a) Power profile.

(b) Temperature profile.

Figure 11: Results of control rod operation strategy St_solid at day 233.

was finally proposed (starting from the outer layer): 45%, 33.6%, 14.3%, and 7.1%. The structure of a control rod is presented in Figure 12. Later layers are referenced by Roman numbers I, II, III, and IV, respectively. This structure was tested for the St_opt strategy, as described in Table 7.

Table 6 presents the worth of each radial layer of control rods in each group corresponding to control rod parts operated in the St_opt strategy and the reactivity swings thus obtained. Every reactivity worth value is calculated as the difference in reactivity of the fresh core with all rods completely withdrawn and reactivity of the core with single specific rod parts inserted. The reactivity worth of the B4C radial layer is much higher than the corresponding reactivity swing in St_opt; however, it should be noted that the method of determining the worth influences the results [41]. The worth of tungsten radial layers decreases as the volumetric fraction of the radial layer decreases. Nevertheless, there is an almost opposite tendency in the case of reactivity swings.

The results of the optimal strategy with structured rods are shown in Figure **??**. With a given control rod structure and operation strategy, axial power oscillations were not eliminated but significantly reduced. In order to visualize the effect of the application of structured control rods, the power profile with minimum power peaking factor is presented in Figure 14a, and the corresponding temperature profile in Figure 14b.

The power peaking factor in the St_opt strategy is the highest in the beginning of the reactor operation, and the lowest in the middle of the operation. However, one can observe that the power peaking factor fluctuates in the last second half of the operation when only external control rods are in the core. Moreover, despite high differences in the amount of the absorber in each control rod layer, the reactivity

Table 6: The worth of control rod parts and the reactivity swings in St_opt.

| **Control Rods Group** | **Radial Layer** | **Reactivity Worth of the Control Rod part [pcm]** | **Corresponding Reactivity Swing in St_opt [pcm]** |
|---|---|---|---|
| All | $B_4C$ | 36735 | 7337 |
| A | I | 3049 | 942 |
| | II | 2667 | 1851 |
| | III | 1805 | 1998 |
| | IV | 866 | 2008 |
| B | I | 3154 | 1266 |
| | II | 2567 | 1879 |
| | III | 1794 | 2125 |
| | IV | 906 | 2025 |
| C | I | 4495 | 1950 |
| | II | 3166 | 2920 |
| | III | 2396 | 2686 |
| | IV | 1523 | 2477 |
| D | I | 4370 | 2128 |
| | II | 3656 | 3237 |
| | III | 2292 | 3134 |
| | IV | 1239 | 2672 |

Table 7: Specification of St_opt control rod operation strategy.

| **Day, CR Group** | **3, A** | **8, A** | **15, A** | **25, A** | **35, A** | **45, A** | **55, A** | **65, A** |
|---|---|---|---|---|---|---|---|---|
| **Withdrawn CR Layer** | I | I | I | I | II | II | II | II |
| **Withdrawn part [%]** | 25% | 50% | 75% | 100% | 25% | 50% | 75% | 100% |
| **Day, CR Group** | **72, A** | **79, A** | **86, A** | **93, A** | **98, A** | **103, A** | **108, A** | **113, A** |
| **Withdrawn CR Layer** | III | III | III | III | IV | IV | IV | IV |
| **Withdrawn part [%]** | 25% | 50% | 75% | 100% | 25% | 50% | 75% | 100% |
| **Day, CR Group** | **118, B** | **123, B** | **128, B** | **133, B** | **138, B** | **143** | **148, B** | **153, B, IV** |
| **Withdrawn CR Layer** | I | I | I | I | II | II | II | II |
| **Withdrawn part [%]** | 25% | 50% | 75% | 100% | 25% | 50% | 75% | 100% |
| **Day, CR Group** | **158, B** | **163, B** | **168, B** | **173, B** | **178, B** | **183, B** | **188, B** | **193, B** |
| **Withdrawn CR Layer** | III | III | III | III | IV | IV | IV | IV |
| **Withdrawn part [%]** | 25% | 50% | 75% | 100% | 25% | 50% | 75% | 100% |
| **Day, CR Group** | **198, C** | **203, C** | **208, C** | **213, C** | **218, C** | **223, C** | **228, C** | **233, C** |
| **Withdrawn CR Layer** | I | I | I | I | II | II | II | II |
| **Withdrawn part [%]** | 25% | 50% | 75% | 100% | 25% | 50% | 75% | 100% |
| **Day, CR Group** | **238, C** | **243, C** | **248, C** | **253, C** | **258, C** | **263, C** | **268, C** | **273, C** |
| **Withdrawn CR Layer** | III | III | III | III | IV | IV | IV | IV |
| **Withdrawn part [%]** | 25% | 50% | 75% | 100% | 25% | 50% | 75% | 100% |
| **Day, CR Group** | **278, D** | **284, D** | **290, D** | **296, D** | **302, D** | **308, D** | **314, D** | **320, D** |
| **Withdrawn CR Layer** | I | I | I | I | II | II | II | II |
| **Withdrawn part [%]** | 25% | 50% | 75% | 100% | 25% | 50% | 75% | 100% |
| **Day, CR Group** | **326 , D** | **332 , D** | **338, D** | **344, D** | **350, D** | **356, D** | **362, D** | **368, D** |
| **Withdrawn CR Layer** | III | III | III | III | IV | IV | IV | IV |
| **Withdrawn part [%]** | 25% | 50% | 75% | 100% | 25% | 50% | 75% | 100% |

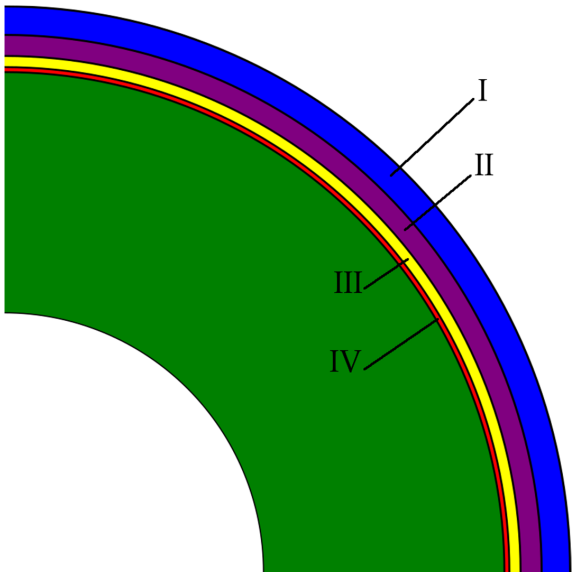


Figure 12: Figure 3. Visualization of the volumetric fractions of the radial layers of the control rods.The innermost central section (green) is made of B4C dispersed in graphite, while the others are made of tungsten. [19]

swing did not differ significantly, ensuring proper control of reactivity.
It can be seen that the flattened power profile results in an overall reduction of temperature in the core, ensuring the safe operation of the reactor.

The power peaking factor in the St_opt strategy is the highest in the beginning of the reactor operation, and the lowest in the middle of the operation. However, one can observe that the power peaking factor fluctuates in the last second half of the operation when only external control rods are in the core. Moreover, despite high differences in the amount of the absorber in each control rod layer, the reactivity swing did not differ significantly, ensuring proper control of reactivity.

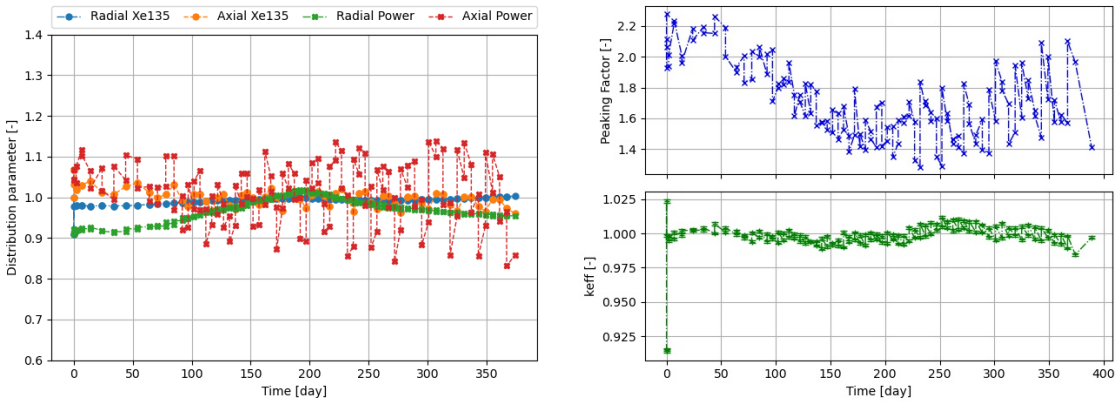


(a) Distribution parameters evolution. (b) Power peaking factor and $k_{eff}$ evolution

Figure 13: Results of control rod operation strategy St_opt.

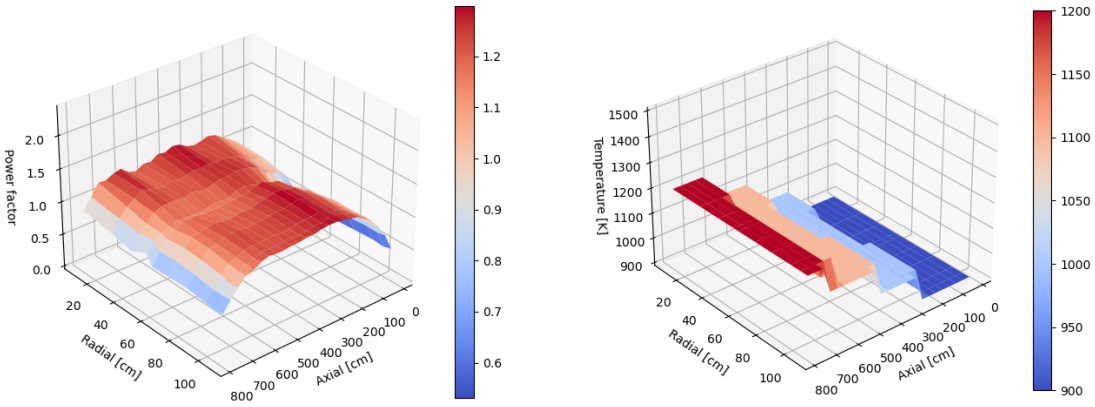


(a) Power profile.

(b) Temperature profile.

Figure 14: Results of control rod operation strategy St_opt at day 227.

# 5 Design of the conjugated heat transfer model on HTGR fuel rod

As it is stated in the IAEA report [44], CFD can support full core analyses by performing more detailed calculations of specific locations in the core. This approach can be utilized in the case of specific fuel rods of HTGRs, as it is essential to estimate the maximum temperature of the fuel. In this section, the basics of CFD will be presented, as well as the specification of applied tools and a detailed description of the CFD model, which is based on a single fuel column of the full core model presented in the previous chapter. Although CFD modeling gives many possibilities in detailed calculations, it was not fully utilized in the work, as a few simplifications were made:

- No by-pass flow.
- No cross flow.
- Compressible flow of the coolant.
- Lack of dependence of properties of solid materials on irradiation.

The above simplifications were applied due to technical difficulties. Thus, the research presented in the work should be continued in the future in order to account for the enumerated phenomena. However, in order to reduce errors resulting from the last simplification, the work was focused on the initial state of the reactor.

## 5.1 Introduction to CFD

CFD is a branch of fluid mechanics that involves the numerical simulation of fluid flow and heat transfer phenomena. It utilizes mathematical models and algorithms to solve the governing equations of fluid motion and provides insights into the behavior of fluids in various engineering and scientific applications.

The fundamental equations governing fluid flow are the Navier-Stokes equations, which describe the conservation of mass, momentum, and energy. These equations are a set of partial differential equations that relate the velocity, pressure, density, and temperature of a fluid to its motion and thermodynamic properties.

One advantage using CFD is that it is possible to obtain detailed local information on the simulated system. In a fluidized bed it is possible to simulate not only the conversion but also the local temperature, the entrainment of particles,

the backmixing and bubble formation. This detailed information will help by building a qualitative understanding of the process, and a parameter study can reveal additional information such as the bottle necks and the operational limits of the equipment [2].

The CFD process involves several steps:

- Problem Definition: The first step is to clearly define the problem and establish the goals of the simulation. This includes specifying the geometry of the system, the fluid properties, boundary conditions, and any other relevant parameters.

- Discretization: The continuous fluid domain is divided into a finite number of discrete elements or cells using a grid or mesh. This is known as the discretization process, and it forms the foundation of CFD simulations. Different types of grids, such as structured grids (e.g., Cartesian or cylindrical) or unstructured grids (e.g., triangular or tetrahedral), can be used depending on the complexity of the problem.

- Governing Equation Discretization: The next step involves approximating the governing equations (e.g., Navier-Stokes equations) in discrete form for each cell in the grid. This is typically done using finite difference, finite volume, or finite element methods, which convert the partial differential equations into a set of algebraic equations.

- Numerical Solution: The discrete algebraic equations are solved iteratively using numerical techniques. The choice of solver depends on the specific problem and the numerical scheme used. Common solvers include the pressure-velocity coupling technique, such as the Semi-Implicit Method for Pressure Linked Equation (SIMPLE) algorithm, which ensures the satisfaction of mass conservation.

- Boundary Conditions: Appropriate boundary conditions are applied to the fluid domain to mimic the real-world scenario. These conditions define the fluid behavior at the boundaries of the computational domain and include specifications such as inlet velocity, pressure, temperature, and wall conditions (e.g., no-slip or free-slip).

## 5.2 Geometry and mesh

The *chtMultiRegionFoam* solver was used for CFD calculations and is dedicated to steady or transient fluid flow and solid heat conduction, with conjugate heat transfer

between regions, buoyancy effects, turbulence, reactions, and radiation modeling. The solver employs a discrete solution approach. This implies that the equations for each variable defining the system are solved sequentially and the answers are included in the ensuing equations. The coupling between a liquid and a solid uses the same technique: To specify the boundary conditions for the temperature in the fluid, the equations for the fluid are first solved using the temperature of the solid from the previous iteration. The boundary condition for the solid temperature is then defined by solving the equation for the solid using the fluid's temperature from the previous iteration. Iterations of this process are carried out until the specified convergence is achieved. [7]. The model developed for coupled calculations consists of four regions, three solids, and one fluid. Solid regions are the fuel, the graphite sleeve (referred further as the sleeve), and the graphite matrix (referred further as the matrix). The fluid region is coolant. The fuel, sleeve, and coolant are concentric annuli incorporated into the matrix hexagon. However, the top and bottom parts of the fuel annulus are replaced with the sleeve region. This was done to represent plugs at the ends of each fuel rod. The overview of the geometry is shown in Figure 15, where the fuel, the sleeve, the coolant, and the matrix are represented with grey, blue, red, and green colors respectively. The mesh spacing in the vertical direction is presented in Figure 16 on a section of the inner part of the rod. The maximum aspect ratio in the mesh is 32.7 and the maximum skewness is 0.07.

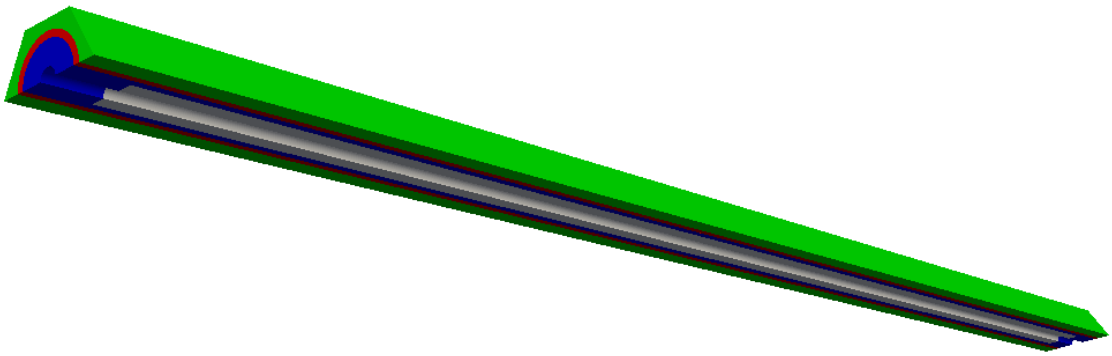

Figure 15: Overview of the geometry of the OpenFoam model.

In order to reduce computational requirements, the geometry was cut in half vertically and the symmetry boundary condition was applied on the cut surfaces. The mesh in all regions is uniform in the vertical direction, but it is condensed near the borders dividing regions, as well as external borders in horizontal directions. The mesh size in the fuel region was set in a way that the biggest cell mesh is comparable in volume with a TRISO particle. In total, the mesh consists on 5654400 vertices. In CFD it is important to take into consideration the influence of shear stresses near

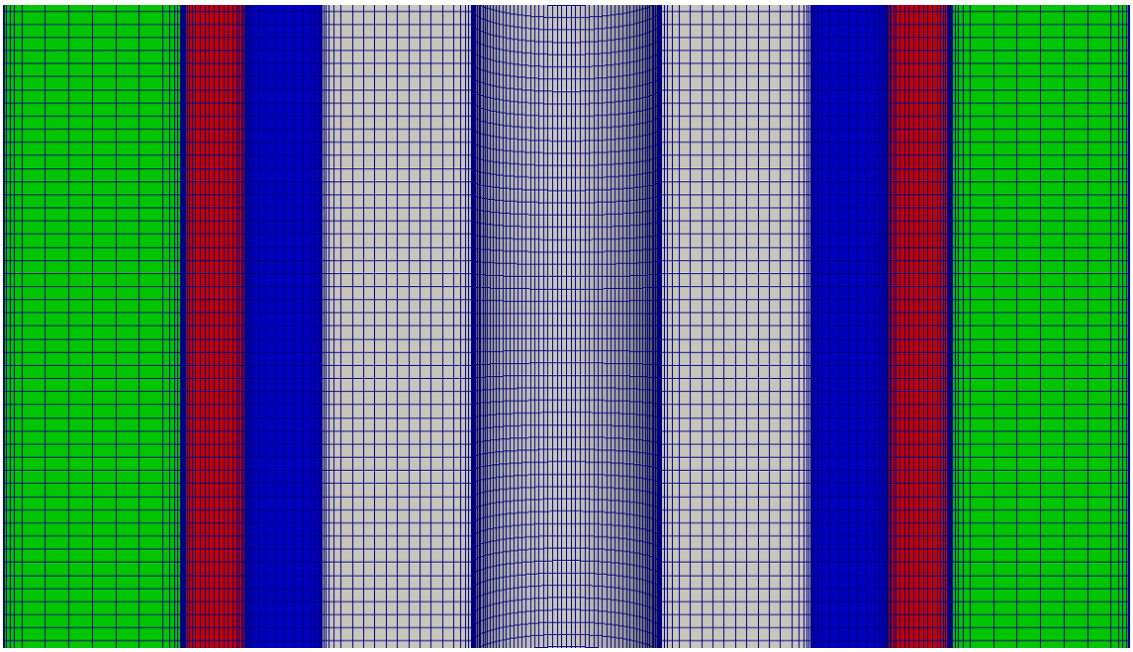

Figure 16: The mesh on a vertical cross-section of the OpenFoam model.

the wall, thus the location of the outermost mesh nodes in the coolant region was set to satisfy the parameter y+=1. Normally, mesh sensitivity analyses should be performed in order to determine adequate mesh density. However, it was not done in this thesis due to the time consumption of this procedure. Moreover, the CFD analyses themselves were not the exact objective of the thesis. Nevertheless, the author is aware that this should be done in future work.

## 5.3 Properties of the CFD model

The model was set in steady-state mode, thus the SIMPLE [39] algorithm was used in the coolant region. The k-omega SST model was used for turbulence simulation as it provides a better prediction of flow separation than most Reynolds Averaged Navier-Stokes (RANS) models, and it has high accuracy to expense ratio [43]. The dependence of materials on the temperature was included using tabulated data from equations given in [3]. For the sleeve and the matrix regions thermal conductivity and specific heat were obtained with formulas for the grade H-451 graphite, equations 3 and 4 respectively.

$$\kappa_G = 3.28248 \cdot 10^{-5} T^2 - 1.24890 \cdot 10^{-1} T + 1.692145 \cdot 10^2 \tag{3}$$

$$\begin{aligned} C_{pG} = (0.54212 - 2.42667 \cdot 10^{-6} T - 90.2725 T^{-1} - 43449.3 T^{-2} + \\ + 1.59309 \cdot 10^7 T^{-3} - 1.43688 \cdot 10^9 T^{-4}) * 4184 \end{aligned} \tag{4}$$

The fuel region consists of several different materials due to the presence of TRISO particles incorporated in graphite. The heat conductivity and specific heat of the kernel material, $UO_2$, are obtained from equations (5) and (6) respectively.

$$\kappa_{UO_2} = \frac{115.8}{7.5408 + 17.692 \cdot \frac{T}{1000} + 3.6142 \cdot \frac{T}{1000}^2} + 7410.5 \cdot \frac{T}{1000}^{-5/2} e^{\frac{-16.35}{\frac{T}{1000}}} \quad (5)$$

$$C_{pUO_2} = 302.27 \cdot \frac{548.68}{T^2} + 8.741 \cdot 10^7 \cdot 18531.7 \frac{e^{\frac{-18531.7}{T}}}{T^2} + 2T \cdot 8.463 \cdot 10^{-3} \quad (6)$$

In case of porous carbon and pyrolitic carbon, equations (7) and (8) were used for their thermal conductivities respectively. Equation (4) was applied for specific heat in both of the above cases, the same as in case of the grade H-451 graphite.

$$\kappa_P C = 122.15 T^{-0.574} [\frac{\rho_{PC}}{2.2 \cdot (1930 - \rho_{PC}) + \rho_{PC}}] \quad (7)$$

$$\kappa_P yC = 244.3 T^{-0.574} [\frac{\rho_{PyC}}{2.2 \cdot (1930 - \rho_{PyC}) + \rho_{PyC}}] \quad (8)$$

Thermal conductivity and specific heat of the SiC are obtained from equations (9) and (10) respectively.

$$\kappa_{SiC} = \frac{17885}{T} + 2 \quad (9)$$

$$C_{pSiC} = 925.65 + 0.3772T - 7.9259 \cdot 10^{-5} T^2 - \frac{3.1946 \cdot 10^7}{T^2} \quad (10)$$

However, accurate representation of each material in the mesh would not only be a tremendous task but would also require enormous computational effort during simulation. Thus, a simplification of the homogenization of materials was provided. Thermal conductivity and specific heat of the homogenized fuel material were calculated as the weighted average of $UO_2$, PC, PyC, SiC, and graphite, where respective mass fractions were used as weights. In the same way, the density of the homogenized fuel was obtained, referred further as to effective density. Mass fractions, densities, and effective density are presented in Table 8.

Thermophysical properties of fluids depend not only on temperature but also on pressure. In the work, the thermal conductivity of the helium coolant was obtained from equation (11).

$$kappa_{He} = 2.682 \cdot 10^{-3} (1 + 1.123 \cdot 10^{-8} p) T^{0.71(1 - 2 \cdot 10^{-9} p))} \quad (11)$$

Table 8: Densities of materials in the OpenFoam model.

| Material | $UO_2$ | PC | PyC | SiC | Graphite | Effective |
|---|---|---|---|---|---|---|
| Mass Fraction [%] | 21.2 | 1.4 | 5.2 | 3.6 | 68.6 | 100 |
| Density [$\frac{kg}{m^3}$] | 10970 | 970 | 1900 | 4210 | 1740 | 3782 |

Dynamic viscosity of the coolant was obtained from equation (12).

$$\mu_{He} = 3.674 \cdot 10^{-7} T^{0.7} \tag{12}$$

The specific heat capacity and density of the coolant $C_{pHe}$ was set to constant values 5195 $\frac{J}{kgK}$ and 4.2 $\frac{kg}{m^3}$ respectively.

Heat transfer by radiation was simulated using the Discrit Ordinance Method (DOM) [12], and the emissivity of the graphite was assumed to be 0.8 [46].

## 5.4 Boundary conditions

As mentioned earlier, half of a fuel rod with a surrounding coolant channel and graphite matrix is modeled by applying the symmetry boundary condition. This approach reduces by half the required computational domain, and in consequence, computational requirements. Thus, it is possible to model each individual fuel rod from the Go_HTR model presented earlier. Taking into account the division of rods into radial burnable zones used there, it can be concluded that each rod is adjacent to at least two rods from the same zone and other rods from at most two other zones. The resulting symmetry requires a maximum of three outer boundaries. A constant heat flux (Neumann boundary condition) or a constant temperature (Dirichlet boundary condition) can be assumed at each boundary separately. The fluxes or temperatures can be read from another program, such as the POKE mentioned earlier.

The gaseous void in the center of the fuel rod is not included in the mesh. Instead, the adiabatic boundary condition is applied at the inner side of the fuel. The assumption of lack of heat exchange between fuel and the void is justified since there is no forced flow in the void as it is closed from all sides, horizontally with fuel and vertically with graphite plugs. Thus, as there is no heat transfer by convection, it is assumed that the void is in thermal equilibrium with the inner side of the fuel. A geometrical simplification was provided that parts of graphite plugs are also not included in the geometry. Enumerated boundaries are presented in Figure 17 on

the mesh horizontal cross-section. The blue part represents the graphite sleeve with plug, the red represents coolant and the green represents the graphite matrix.

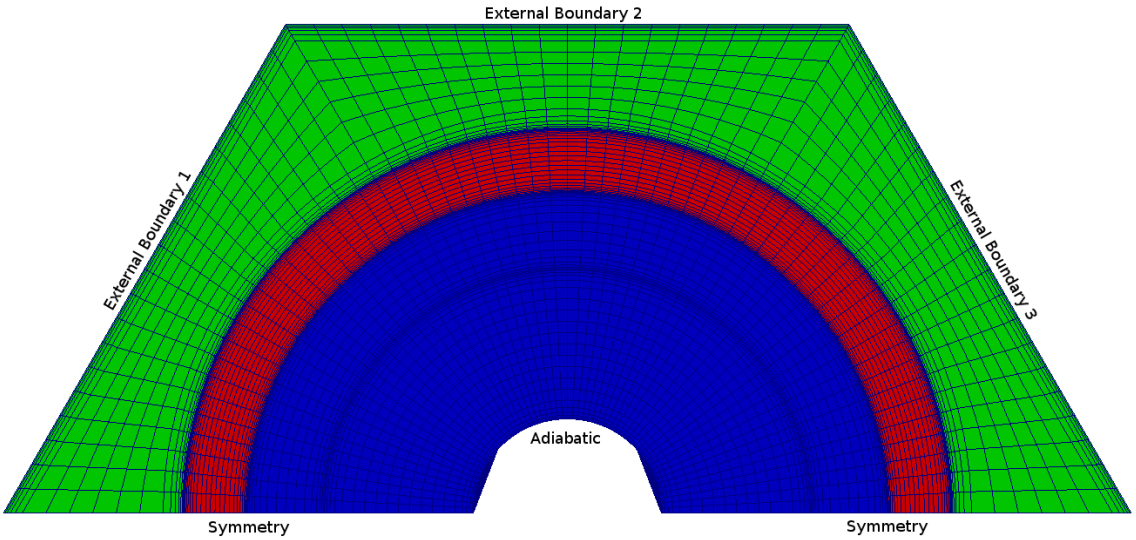


Figure 17: The mesh on a horizontal cross-section and boundary conditions of the OpenFoam model.

Regarding the top and bottom boundaries of solid regions, also adiabatic boundary condition was applied. This is not the most realistic approach. However, it is a conservative assumption regarding the top boundary since heat flux from the graphite plug to the upper plenum of the reactor is expected. Regarding the bottom part of the geometry, a small heat flux can be expected from the fuel rod below, but this issue should be resolved with the expansion of the domain to the entire fuel rod column, which is not within the objective of this research.

The inlet is situated on the top boundary of the coolant region. Inlet temperature and pressure can be obtained directly from POKE. The inlet velocity can be calculated from the inlet mass flow rate in certain coolant channels obtained from POKE, using Equation (13), where the outer and inner radii of the coolant channel were applied.

$$U = \frac{\dot{m}}{\rho_{He}\pi(r^2_{coolant} - r^2_{sleeve})} \tag{13}$$

The outlet is situated at the bottom boundary of the coolant region. The boundary condition for temperature is the *inletOutlet*, which is a mixed boundary condition that in case of a positive flux (out from domain) applies the *zeroGradient* condition, and in case of a negative flux (into of domain) applies fixed inlet value [48]. In case of described case, a negative flux at the outlet boundary is not expected, thus practically an adiabatic boundary condition is appied. Fixed outlet flow

rate is set to be the same as inlet, and the outlet pressure is calculated.

Internal borders between solid regions of sleeve and matrix, and fluid coolant region are *compressible::turbulentTemperatureRadCoupledMixed*, which enables heat transfer by radiation. Moreover, a thin helium gap imposing a thermal resistance layer of 0.0125 cm [23] was included within the internal boundary condition *compressible::turbulentTemperature*
*CoupledBaffleMixed* between the fuel and the sleeve region.
The most important part of this work is the determination of the detailed temperature distribution in the fuel. Therefore, a simplified model of heat transport in the fuel and sleeve was made, taking into account the aforementioned helium gap, for validation with the distribution obtained analytically. The simplified model consists only of cylindrical regions of the fuel and sleeve, with a constant temperature at the outer boundary of the sleeve. The analytical distribution was obtained by solving the Poisson equation for the fuel and the Laplace equation for the gap and the sleeve. The analytical solution in cylindrical coordinates is Equation (14) for sleeve region, Equation (15) for the gap and Equation (16) for the fuel region.

$$T(r) = T_{sleeve} + \frac{P(r_{fuel}^2 - r_{void}^2)}{2\kappa_C} \ln(\frac{r_{sleeve}}{r}) \tag{14}$$

$$T(r) = T_{sleeve} + P(r_{fuel}^2 - r_{void}^2)(\frac{\ln(\frac{r_{sleeve}}{r_{gap}})}{2\kappa_C} + \frac{\ln(\frac{r_{gap}}{r})}{2\kappa_{He}}) \tag{15}$$

$$T(r) = T_{sleeve} + P(r_{fuel}^2 - r_{void}^2)(\frac{\ln(\frac{r_{sleeve}}{r_{gap}})}{2\kappa_C} + \frac{\ln(\frac{r_{gap}}{r})}{2\kappa_{He}}) + \frac{Pr_{void}^2}{2\kappa_{fuel}} \ln(\frac{r_{fuel}}{r}) + \frac{P(r_{fuel}^2 - r^2)}{4\kappa_{fuel}} \tag{16}$$

The valudation was performed assuming the outer sleeve boundary temperature of 500K and $\kappa_{He}$ and power density in the fuel equal 3 kW. Results of the validation are presented in Figure 18.

Validation shows good agreement between analytical and calculated results. However, the limitation of the OpenFoam is that it is for now impossible to set the dependence of thermal conductivity of the thermal resistance layer on temperature. Instead, the value needs to be fixed, which is a simplification.

## 5.5 Results

Calculations were made for a fuel rod located in the uppermost block of the central fuel block column. The power density, inlet temperature, pressure, and mass flow were obtained from the POKE results for beginning of the operation of the reactor.

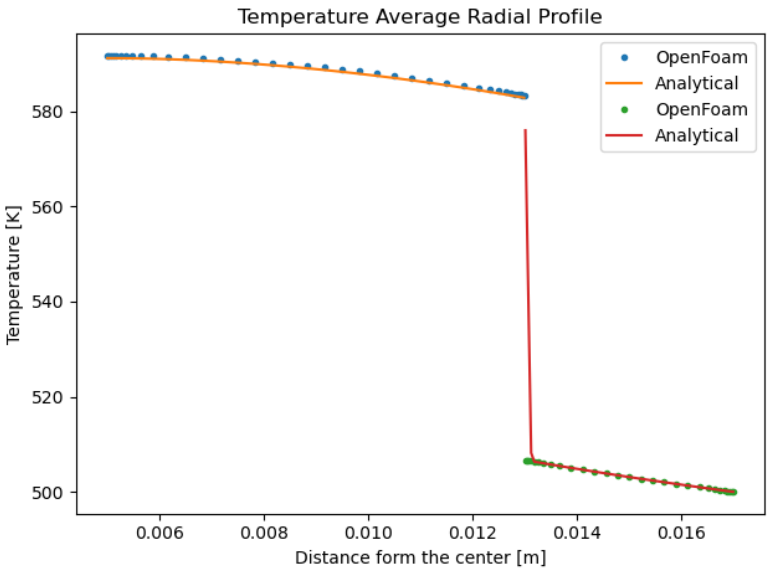


Figure 18: Validation results for simplified heat transfer model in the fuel, gap, and sleeve.

Thus, the power density is 77.26 $\frac{MW}{m^3}$, the inlet temperature is 395 K and inlet pressure is 4 MPa, mass flow is 0.0358 $\frac{kg}{m^3}$, which corresponds to the inlet velocity of 41.08 $\frac{m}{s}$. The thermal conductivity of the thermal resistance layer between the fluid and the sleeve was set to 0.31072 $\frac{W}{mK}$, which corresponds to helium at 700K and 4 MPa [37]. The results of the axial and radial temperature profiles and pressure profile are presented in Figure 19, Figure 20, and Figure 21 respectively.

The data for Figure 19 were taken from the surface perpendicular to the *External Boundary 2* in the middle of its width. The *Fuel Maximum* data is taken along the axis at the radius of 0.5 cm, which is at the inner adiabatic boundary. The *Fuel Central* data is taken along the axis at a radius of 0.9 cm, which is the middle of the fuel region. Analogically, the *Sleeve Maximum* is taken from the internal border between the fuel and the sleeve at a radius of 1.3 cm, and the *Sleeve Central* is in the middle of the sleeve region at a radius of 1.5 cm. Further, the *Coolant Maximum* data is taken from the internal boundary between the sleeve and the coolant, which is at a radius of 1.7 cm. The *Coolant Central* and the *Matrix Central* are taken from the middle of the coolant and the matrix regions, at radii of 1.875 cm and 2.3 cm respectively. The data of Figure 20 are taken from the same surface, but at an axis at a height of 50 cm, which is roughly the center of the rod. One can see that the temperatures of solids at the inlet are close to the inlet temperature of the coolant. However, the influence of the presence of graphite plugs over and under the fuel is visible since there is a rapid change of temperature at the internal borders between the plugs and the fuel. The temperature in the fuel region gradually increases in

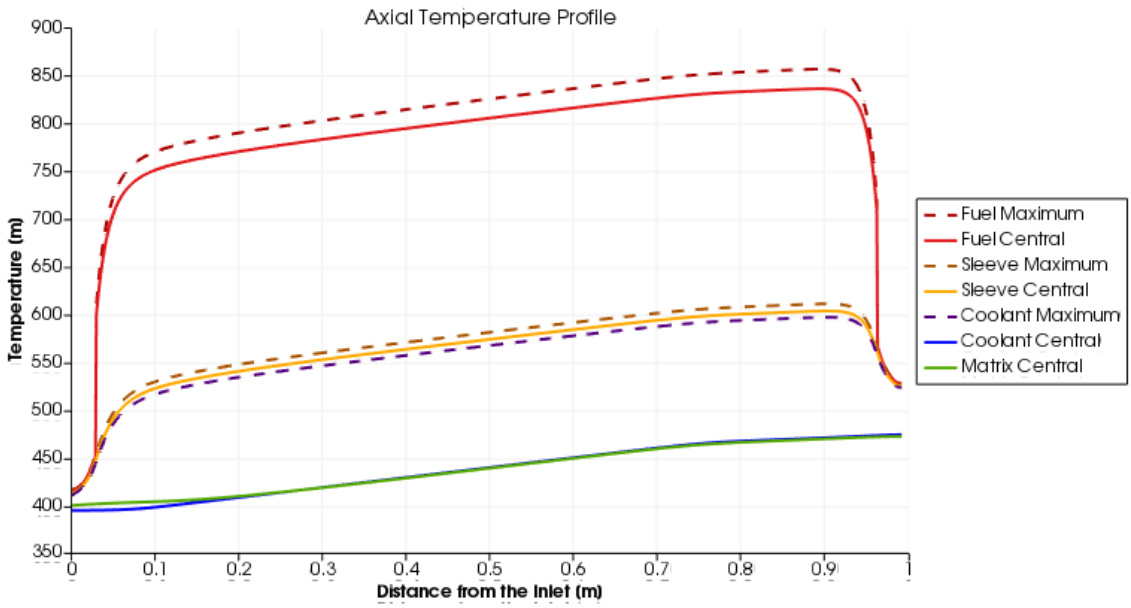


Figure 19: Axial temperature profile.

depth, achieving a maximum of 857.014 K. Similar behavior is reflected in the sleeve region, but temperatures are significantly smaller due to the gaseous gap between the fuel and the sleeve. The temperature of the coolant is the highest at the sleeve wall and decreases with distance from the sleeve, to the temperature slightly lower than the temperature of graphite.

The pressure decreases linearly with distance from the Inlet, which is expected since by-pass and cross flows are not included [21]. The minimum pressure is 3.98776 MPa.

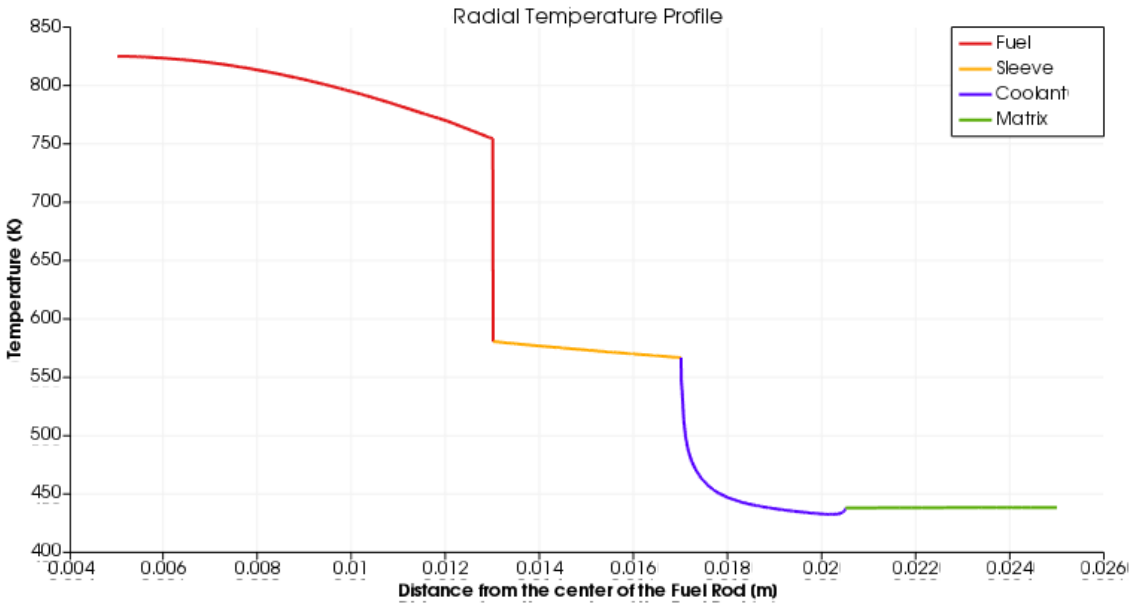


Figure 20: Axial pressure profile.

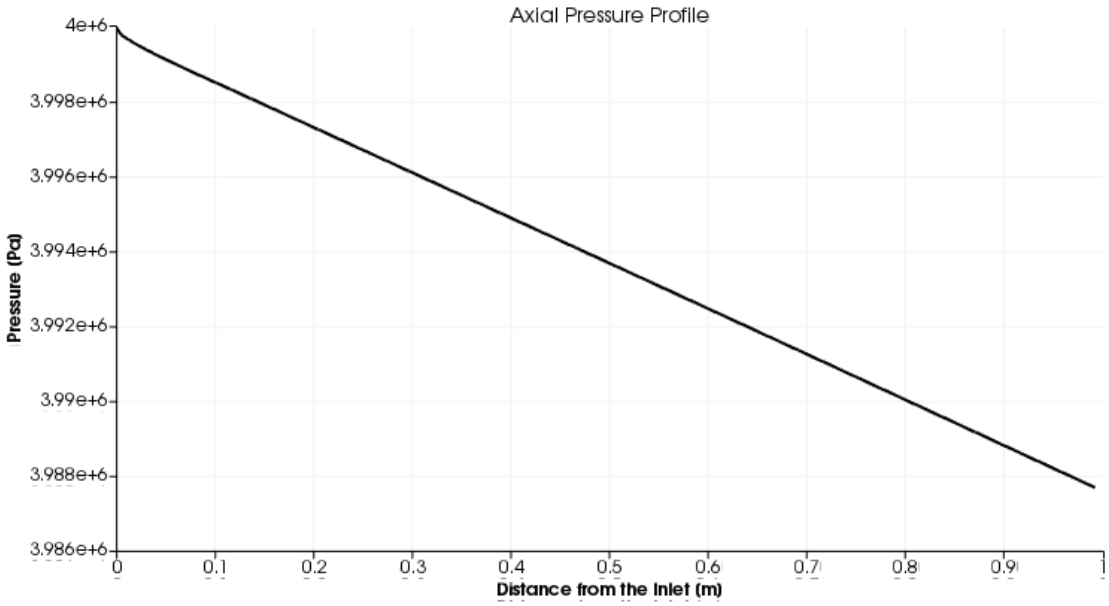


Figure 21: Axial pressure profile.

# 6 Coupled Serpent/OpenFoam calculations

Multi-physics applications were taken into consideration when creating Serpent 2. The majority of temperature and density distributions provided by, for example, thermal hydraulics or CFD solvers can be imported into Serpent using one of the multi-physics interface file formats without loss of detail thanks to the ability to represent arbitrary fine-grained density and temperature distributions. The multi-physics interface is a set of routines, as well as input/output formats intended for easily bringing in detailed temperature and density fields to Serpent and at the same time automatically producing power distributions to be used in coupled codes [22]. To get the converged coupled solution, special procedures are available for managing the iteration between the coupled field solver(s) and the neutronics solver (Serpent). With the help of the global multi-physics interface, temperature and density solutions from any external solvers may be imported quickly. The underlying geometry model can be overlaid with the solution fields (temperature/density) using the multi-physics interface without requiring further input changes (such as specifying several materials with varying temperatures). [8].

## 6.1 Serpent

Serpent is a computational tool developed by the VTT Technical Research Centre of Finland for simulating neutron physics and conducting neutronic calculations. It is a versatile and efficient Monte Carlo reactor physics code widely used in the nuclear engineering community. Serpent utilizes the Monte Carlo method to simulate the behavior of neutrons in complex geometries, providing detailed information on neutron flux, reaction rates, and other relevant parameters [31].

The key features of the Serpent code include:

- Monte Carlo Method: Serpent employs the Monte Carlo method, a stochastic simulation technique, to track individual neutrons through the system being analyzed. It uses random sampling to model the behavior of neutrons, taking into account various physical processes such as scattering, absorption, and fission.

- Geometry Modeling: Serpent allows for the description of complex geometries using a combination of analytical surfaces, such as planes, cylinders, and spheres, and Constructive Solid Geometry (CSG) techniques. This enables the representation of intricate nuclear systems, including reactor cores, fuel assemblies, and other components with a high level of detail.

- Material Definitions: The code supports the specification of material compositions using a variety of methods. These include isotopic compositions, elemental compositions, and density distributions. The serpent also offers a comprehensive library of nuclear data, including cross-section libraries, decay data, and fission yield data, allowing users to accurately model and analyze a wide range of materials and isotopes.

- Neutron Transport: Serpent simulates neutron transport by sampling the interaction of neutrons with materials based on their cross-section data. It tracks the individual neutrons as they undergo scattering, absorption, and fission events, providing statistical estimates of various quantities of interest, such as neutron flux, reaction rates, and power distribution.

- Cross-Section Data: Serpent utilizes cross-section libraries to provide accurate nuclear data for various isotopes and reactions. These libraries contain information about microscopic cross-sections, including total, elastic, inelastic, and capture cross-sections. The serpent can use different types of cross-section libraries, such as continuous-energy libraries or multi-group libraries, depending on the requirements of the simulation.

- Burnup Calculations: Serpent has capabilities for performing burnup calculations, which simulate the depletion of isotopes and the evolution of neutron flux and reaction rates over time. This feature allows users to analyze the long-term behavior of nuclear systems, assess fuel depletion, and study the effects of fuel burnup on reactor performance.

### 6.1.1 Fuel rod in Serpent

Because of the way the Serpent code works, it was necessary to model the entire fuel rod, without being able to reduce the domain, as was done for the OpenFoam calculations in the previous chapter. At the center of the geometry is a cylinder responsible for the helium-filled gas space at the center of the fuel rod. As in the previously discussed calculations, the cylinder is surrounded by concentric rings corresponding in turn to the fuel, the sleeve, and the cooling channel. The whole is placed in a graphite hexagon. To represent the location of the rod in the lattice of rods in the block, a periodic boundary condition was used. However, the explicit stochastic geometry functionality was used for the generation of randomized TRISO arrangements. Dimensions and densities of TRISO layers as well as other materials are the same as in previous calculations. The geometry is presented in Figure 22.

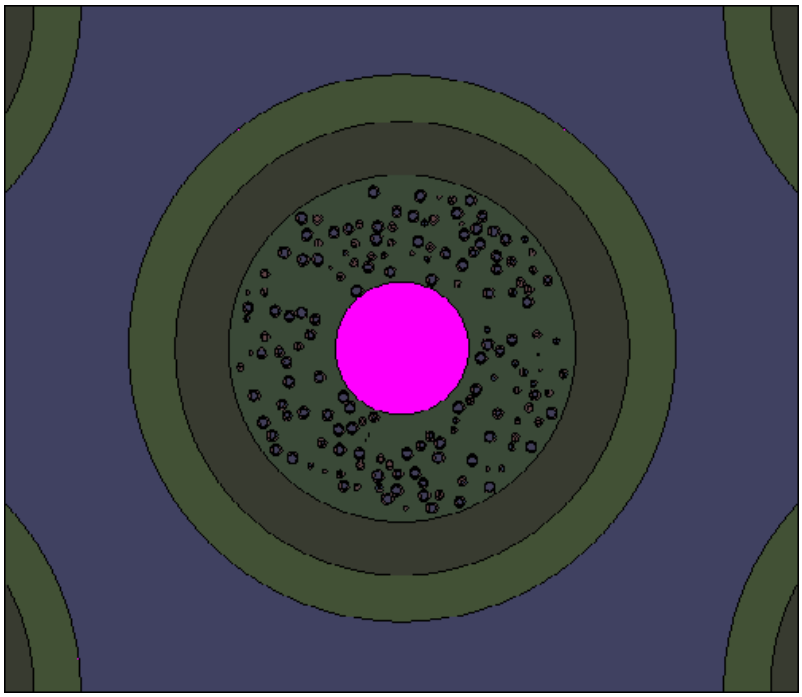

Figure 22: Fuel rod model with random TRISO arrangement in Serpent.

## 6.2 Power discretization for random TRISO particles arrangement

As mentioned in the previous chapter, it is difficult to accurately account for TRISO particles in a CFD model. However, using the ability to define heat sources in individual cells of the OpenFoam mesh, it is possible to represent the heat distribution generated in TRISO particles fairly accurately. In order to perform the power discretization with respect to TRISO particle positions, coordinates of TRISO particle centers are required. Those can be generated with the explicit stochastic geometry, using the Serpent *disperse* option. Then, cell centers of the OpenFoam mesh should be obtained, and that can be done using the *writeMeshObj* applicability. The next step is to calculate the distance between each mesh cell center to each TRISO center. This, of course, is a simple, yet computationally demanding process, as there are easily hundreds of thousands of TRISO particles and millions of mesh cells. One way to optimize such an operation is to first simply calculate the differences between the coordinates of cell and TRISO centers, and perform the calculation of distances only if the differences are sufficiently small. Thus, the distances are calculated only in certain areas around a mesh cell. The minimum calculated distance should then be taken for a mesh cell, and compared to the TRISO kernel and layers dimensions. If the distance is no greater than the radius of the TRISO kernel, the cell can be identified as a kernel, and if the distance is within the range of a TRISO coating

layer, the cell can be identified as a respective layer. If the distance is greater than the external radius of a TRISO particle, then the cell can be identified simply as graphite. With this procedure, it is possible to obtain *materials* file required for the Serpent multi-physics interface type 8 [22]. During the procedure, the mesh cells identified as fuel kernels can be further assigned in the *mapping* file for Serpent multi-physics interface and then used as heat sources in the OpenFoam *fvModels* file.

Since the Monte Carlo method involves collecting collision data from a specific space and averaging the results, high uncertainties are to be expected for too small a space. A single OpenFoam grid cell is usually a small space, so kernel cells should be grouped so that fission data is included in a larger grouping of cells, i.e. a larger space. Such grouping can be performed in the mentioned *mapping* file, and groups of cells are referred further as to power bins. On the other hand, the introduction of power bins can influence the power profile, depending on how the bins are defined. This problem shall be covered in detail in future studies, as in this work the concept is introduced. The bins in this work are defined by the radial and axial position ranges of mesh cell locations. This means that the domain is divided into radial and axial zones, and cells identified as kernels are assigned to individual bins based on their location in a particular zone. The procedure of generation of the power bins is presented in Figure 23. Stage a) shows a horizontal fuel pellet cross-section so that the division in two dimensions can be presented. Stage b) shows the division of the domain into two radial and two axial zones, 4 zones in total, each described with different frame colors (red, green, yellow, and purple). Stage c) shows TRISO kernels assigned to the zones, however, it should be noted that a single kernel can be divided into several zones. It should be understood that fission data taking place in a single kernel is averaged to all kernels in the zone, in order to reduce uncertainties. Finally, stage d) shows the OpenFOAM mesh cells assigned to power bins with the color of the respective zone. It should be understood that all cells within a single power bin have the same value of power density generation.

One can speculate that the accuracy of the power bins generation depends on the sizes of the OpenFOAM mesh cells. This topic also should be studied in the future. However, it is suggested that the maximum cell size should be small enough so that the cell could be inscribed in the TRISO kernel so that no kernel would be omitted during the power discretization.

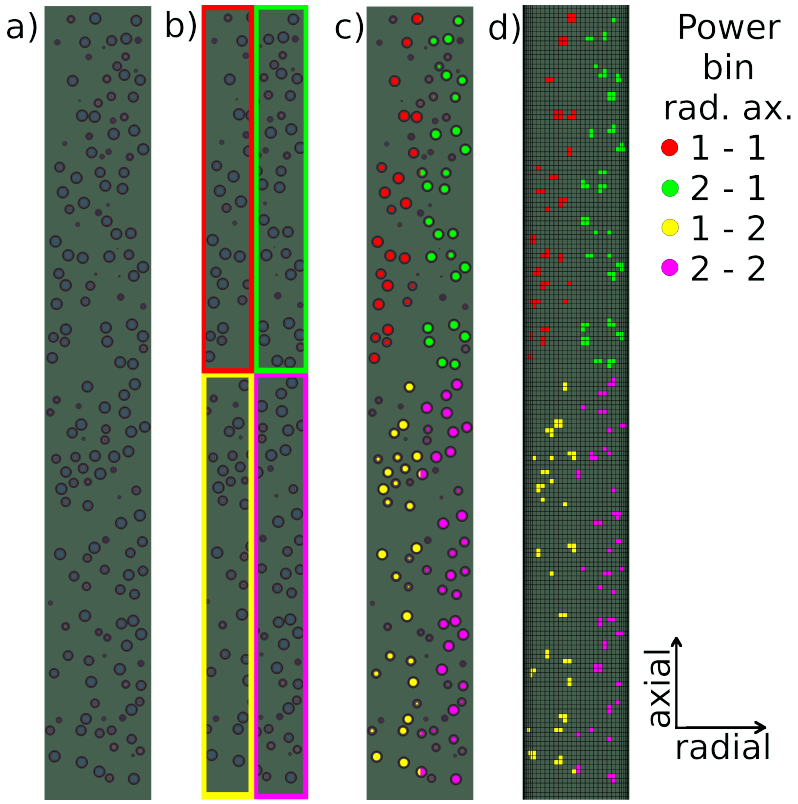


Figure 23: Procedure of power bins generation. a) horizontal fuel pellet cross-section, b) division to power zones, c) assignment of cells identified as TRISO kernels to power bin, d) power bins in the OpenFoam mesh.

### 6.2.1 Coupling with the fuel rod OpenFoam model

To represent the power distribution as adequately as possible taking into account TRISO positions, the model in OpenFOAM was modified. Namely, the mesh was thickened, but the geometry was also reduced to 1 fuel rod so that one external boundary remained. The resulting mesh consists of 14757600 vertices. The symmetry boundary condition was replaced by a cyclic condition. These conditions further map the rod surrounded by rods in the same firing zone, nevertheless, it can no longer be applied to rods surrounded by rods of other zones. The mesh and boundary conditions are presented in Figure 24. To ease the analysis of the results for the purposes of this calculation, the graphite plugs at the ends of the fuel rods were omitted. However, since total power was given in the OpenFoam calculations, the power density may decrease, leading in a further decrease in temperature. This subject needs to be corrected in future work.

Reducing the geometry in OpenFoam relative to the model in Serpent creates the problem that the latter is not completely covered by the temperature mesh. To solve this problem, a minor modification was made to the Serpent source code. A

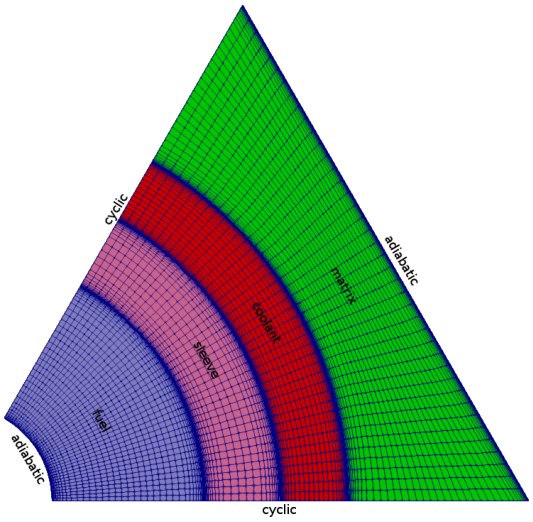


Figure 24: Horizontal cross-section used for Serpent multi-physics interface.

six-fold rotation of the temperature mesh by 60 degrees was introduced. This causes the entire domain to be covered by an angularly repeatable temperature mesh in this particular case. To keep the calculations consistent, modifications were made to the random distribution of TRISO capsules. First, particles that are crossed by cyclic boundaries of the OpenFoam model were removed. Second, analogous to the temperature mesh, the positions of those TRISOs that were covered by the OpenFoam mesh were rotated six times by 60 degrees. The effect of this operation, along with the corresponding mesh, can be seen in Figure 25. Black lines correspond to the borders of rotation operations.

The sequential exchange of input and output files between the Serpent and the external solver forms the foundation of the external coupling. Serpent offers a separate coupled calculation mode where Serpent interacts with an external code to control the solution flow, preventing the need to restart Serpent after each neutron transport solution (and hence necessitating the repetition of all the pre-processing). After each neutronics solution in the coupled computation mode, Serpent will go to sleep and wait for the new interface files [8]. The simplified coupling scheme used in this work is presented in Figure 26. The file preparation part is the initial power discretization described earlier. Power profile update is done by generating a *fvModels* file from the multi-physics interface output file, and the temperature profile is updated by linking temperatures obtained in the last written OpenFOAM results catalog to the interface via *ifc* files.

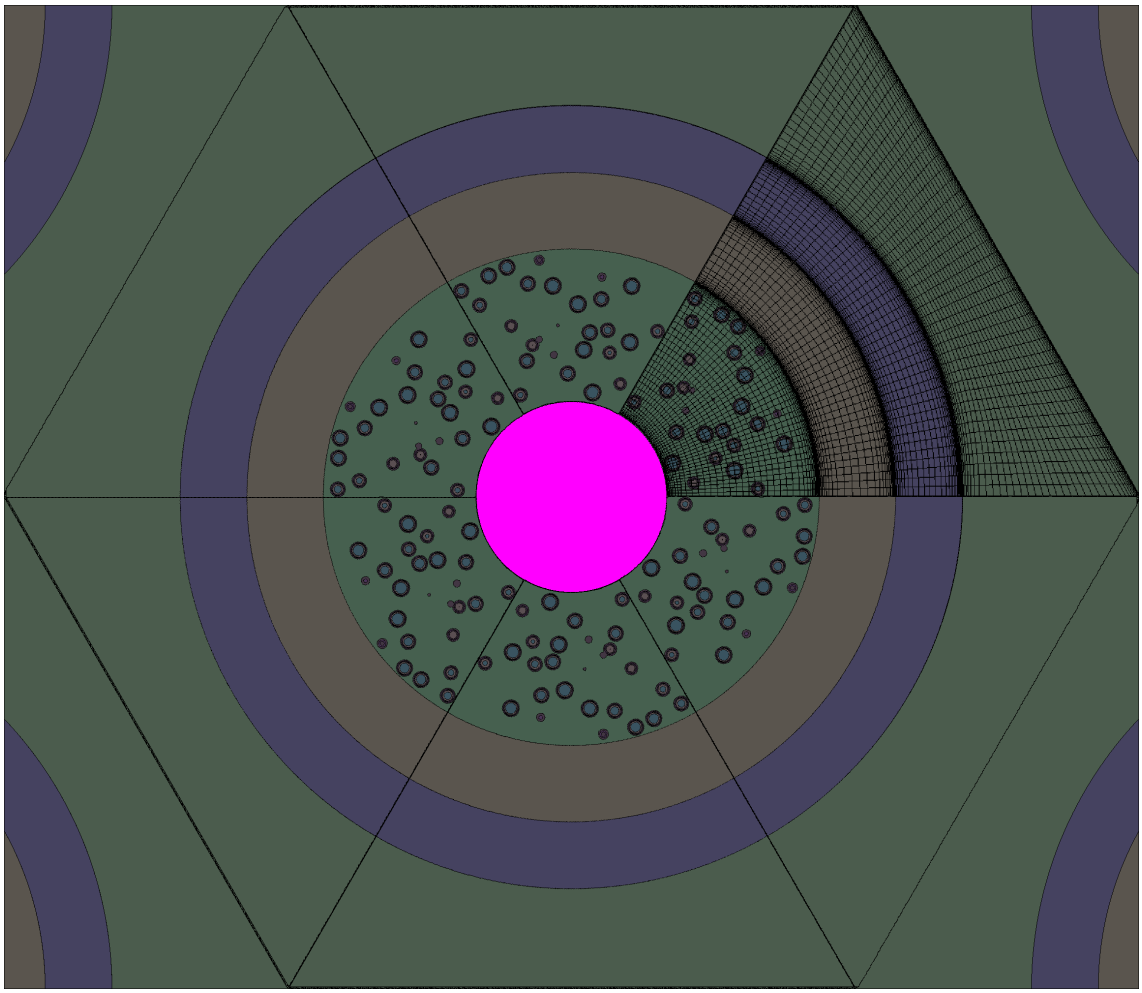

Figure 25: Fuel rod model with modified random TRISO arrangement and OpenFOAM mesh in Serpent.

## 6.3 Results

The initial OpenFOAM calculations were done with uniform power distribution, and based on the resulting temperature profile, several Serpent calculations were run for different power bin arrangements. The number of neutron histories is 12000, 100 active and 20 inactive cycles are simulated. Results of averaged radial and axial power profiles are presented in Figure 27 and Figure 28 respectively. In those figures, *Rad.* is the number of radial bins, *Ax.* is the number of axial bins, *Avg.* $u$ is average power uncertainty, and *pf* is peaking factor.

In order to investigate the accuracy of the mesh cell adjustment to TRISO, a separate power bin is set for all cells that are supposed to represent the graphite in which TRISO particles are dispersed. It would be expected that no power would be generated in the bin. However, due to the fact that hexagonal mesh cannot ideally reflect fuel kernel spheres, it is possible that some fission in the Serpent simulation may appear in a cell that is identified as graphite. In this study, the amount of

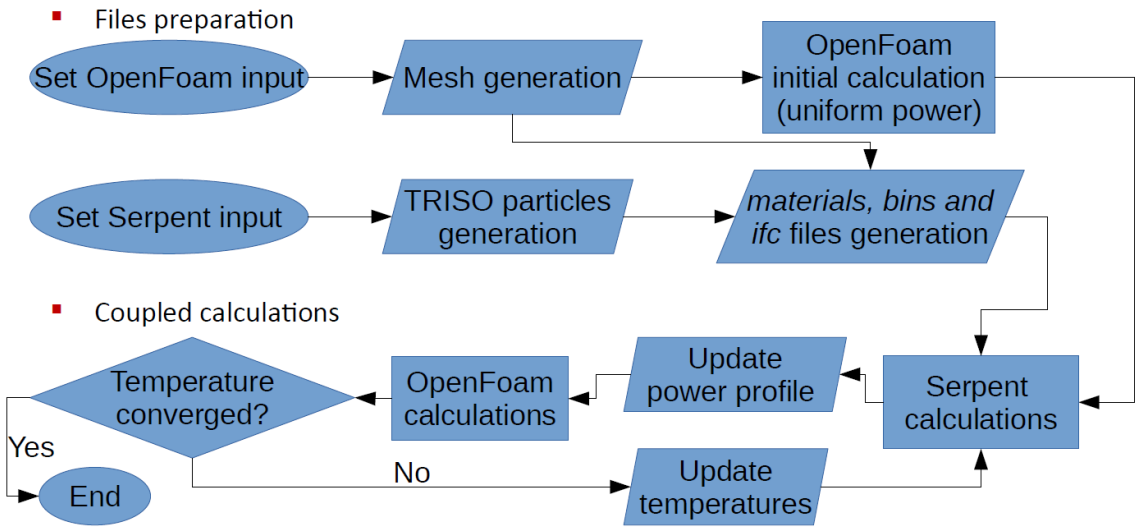


Figure 26: Serpent and OpenFoam coupling block scheme.

power generated in such cells is 5.6% of total power. Nevertheless, this issue could be considered as justified since, in fact, a small fraction of power in thermal reactors is produced in a moderator, and in HTTR it is approximately 5% [45]. It can be noted that in the absence of the use of power binning (i.e., each OpenFoam mesh cell is a separate binning), huge uncertainties of 95% were obtained despite the not inconsiderable neutron population. On the other hand, it can be seen that the fewer the bins, the smaller the uncertainty. Therefore, as few bins as possible should be used to represent the power distribution fairly accurately. However, this is a complicated task that should be carried out in future studies. In the case of averaged radial distributions, one can see a slightly increased power density at the inner and outer edges of the fuel rod. However, no significant differences in power distribution can be seen between the number of radial bins. The axial power distribution reproduces the randomness of the TRISO particle distribution, and again, no significant differences in power distribution between the number of axial bins can be seen. This means that just taking TRISO positions into account has the effect of increasing the accuracy of the power distribution.

A configuration of 5 radial bins and 20 axial bins was selected for further calculations. The used criterion of convergence was that of the temperature difference in each grid cell in the following time steps were not greater than 3 K. The coupling resulted in a more random axial temperature distribution, which corresponds to the randomness of the power distribution. Results are presented in Figure 29 for initial temperature profile from uniform power profile, and in Figure 30 for temperature profile after introducing power discretization. However, the maximum temperature after coupling is 720.4 K, while in case of uniform power distribution it is 709.6 K.

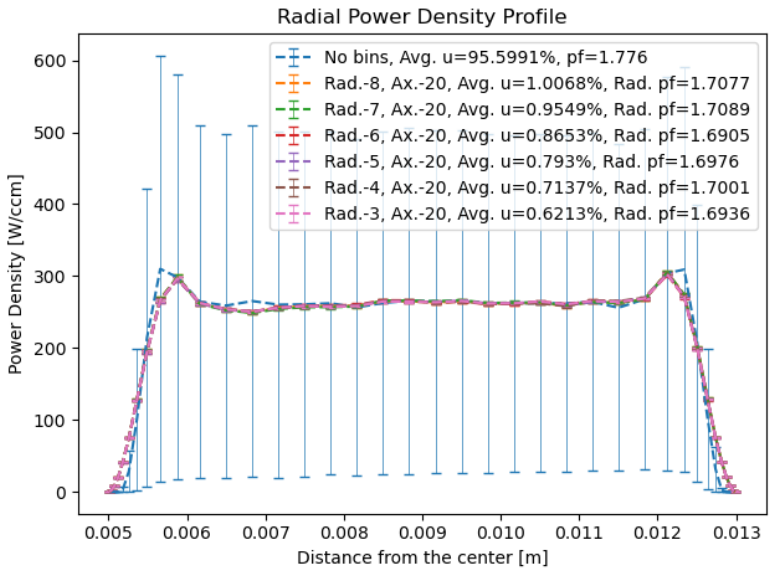


Figure 27: Averaged radial power profiles for several radial power bins arrangements.

This means that implementation of the power discretization showed the temperature higher by a few percent, which can be included in safety margin in case of normal operation of the reactor [27].

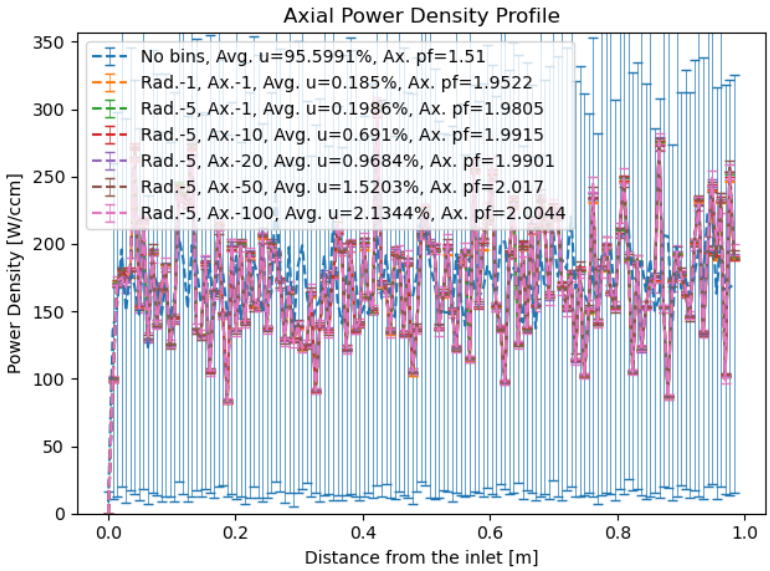


Figure 28: Averaged axial power profiles for several axial power bins arrangements.

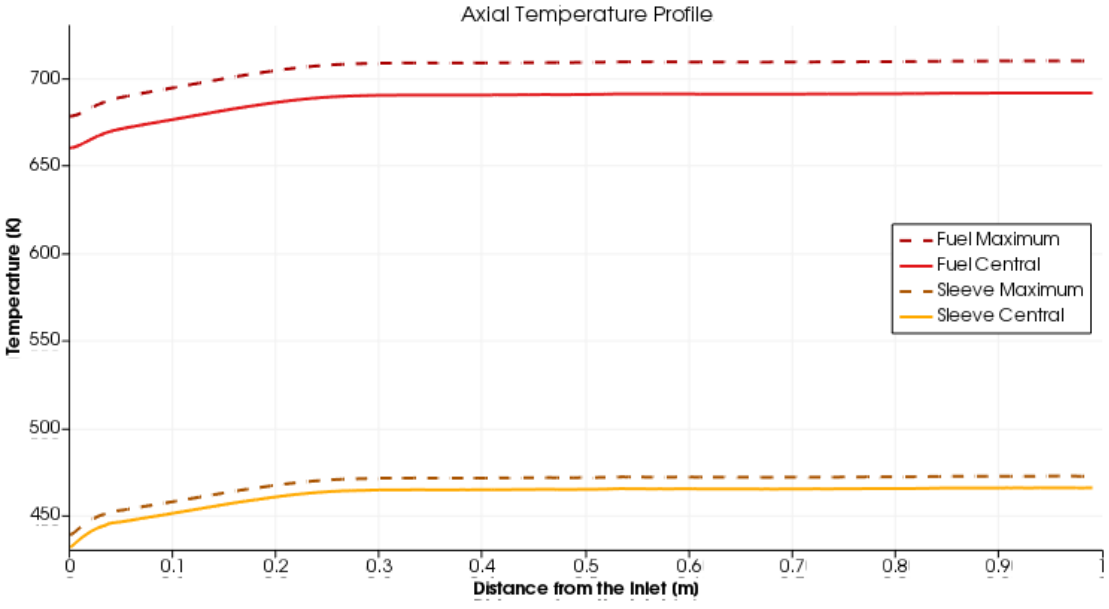


Figure 29: Axial temperature profile after initial OpenFoam calculation with uniform power profile.

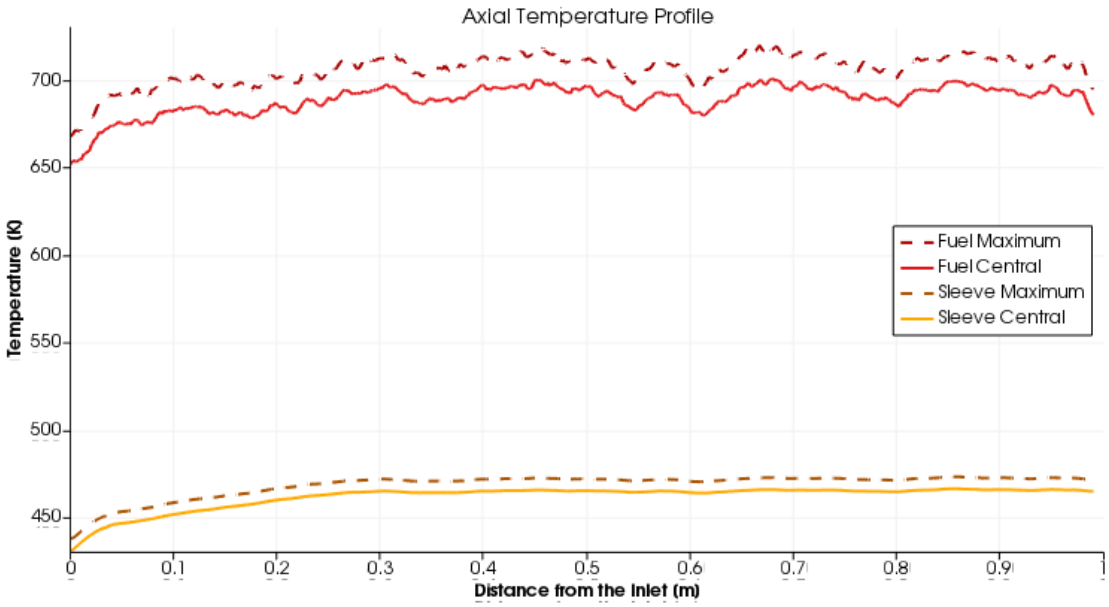


Figure 30: Axial temperature profile after coupled calculation profile.

# 7 Conclusions

This paper presents the characteristics of HTGRs, with a discussion of the history and neutronic, thermo-hydraulic properties and the feedback that occur between them. An example of the use of coupled neutron and thermo-hydraulic calculations using MCB and POKE codes within the PUMA project is further presented. The relationship between power and temperature distributions is then shown based on the Go_HTR core model with structured control rods. The application of this innovative concept allowed for a significant flattening of the power distribution and thus a reduction in the average core temperature, allowing for safer and more efficient operation. The purpose of this dissertation was to demonstrate that local CFD calculations can support analyses of the entire reactor core using coupled thermal-fluid and neutronic calculations. This was accomplished in part by creating a model of a single Go_HTR fuel rod and using power data from the MCB and temperature and flow data from the POKE. Full OpenFoam coupling with MCB and POKE was not achieved here, but a significant portion of it was achieved. Some simplifications were also applied, such as not including by-pass flow and cross-flow, and changes in material properties under irradiation. Research is currently underway to include py-pass and cross flow in CFD calculations, but including them in coupled calculations remains an open topic. Moreover, another challenge is the inclusion of TRISO particle distribution in the CFD model. Accurately mapping TRISO geometry in CFD is a challenging task; nevertheless, this paper develops a method to map the power distribution that considers TRISO distribution. The da method, hereafter referred to as power discretization, assumes that TRISO particles are grouped into power bins. The optimal choice of the number of bins remains an open question, which is a topic for further research. Another issue is the appropriate matching of the OpenFoam mesh, as the accuracy of the representation of the power profile in CFD calculations depends on it, but this too remains for further research. Nevertheless, with an arbitrary selection of 5 radial and 20 axial bins, a coupling of the adjusted OpenFoam model and the corresponding single fuel rod model in Serpent was performed, using a multi-physics interface. The use of power discretization yielded temperatures that were magnified by about 10 K relative to the use of a uniform power distribution. This increase can be considered in the safety limit during normal reactor operation. However, further studies may be required in order to determine the impact of several factors on the maximum temperature. Those factors include the TRISO packing factor, the size of TRISO kernels, and higher power densities.

# References


[1] *Advances in High Temperature Gas Cooled Reactor Fuel Technology*. IAEA-TECDOC-1674. International Atomic Energy Agency, 2012.

[2] Bengt Andersson et al. *Computational Fluid Dynamics for Engineers*. Cambridge University Press, 2012.

[3] *B enchmark of the Modular High-Temperature Gas-Cooled Reactor (MHTGR)-350 MW Core Design*. NEA/NSC/R(2017)4. Nuclear Energy Agency, 2018.

[4] Jerzy Cetnar, Wacław Gudowski and J Wallenius. "MCB: A continuous energy Monte Carlo Burnup simulation code". In: *EUR 18898 EN, OECD/NEA* 523 (1999).

[5] Jerzy Cetnar, Mariusz Kopeć and Mikołaj Oettingen. *Advanced fuel burnup assessments in prismatic HTR for Pu/MA/Th utilization using MCB system*. Monograph of Department of Nuclear Energy Faculty of Energy and Fuels. AGH University of Science and Technology, 2013.

[6] Jerzy Cetnar et al. *Przygotowanie Ró żnych Konfiguracji Rdzenia Pryzmatycznego Reaktora HTGR Na Potrzeby Analizy Ekonomicznej (Unpublished Report in Polish)*. AGH UST, 2020.

[7] OpenFoam. *ChtMultiRegionFoam*. URL: `https://openfoamwiki.net/index.php/ChtMultiRegionFoam`. Accessed: 06.14.2023.

[8] Serpent Wiki. *Coupled multi-physics calculations*. URL: `https://serpent.vtt.fi/mediawiki/index.php/Coupled_multi-physics_calculations`. Accessed: 06.14.2023.

[9] *Design of a High-Temperature Engineering Test Reactor (HTTR), JAERI 1332*. Japan Atomic Energy Research Institute: Ibaraki, 1994.

[10] "DOE fundamentals handbook: Nuclear physics and reactor theory. Volume 1". In: (Jan. 1993). DOI: `10.2172/10144941`. URL: `https://www.osti.gov/biblio/10144941`.

[11] "DOE fundamentals handbook: Nuclear physics and reactor theory. Volume 2". In: (Jan. 1993). DOI: `10.2172/10144945`. URL: `https://www.osti.gov/biblio/10144945`.

[12] ANSYS. Inc. *Discrete Ordinates (DO) Radiation Model Theory*. URL: `https://www.afs.enea.it/project/neptunius/docs/fluent/html/th/node115.htm`. Accessed: 06.09.2023.

[13] C.G. du Toit et al. "A systems CFD model of a packed bed high temperature gas-cooled nuclear reactorA preliminary version of this paper was presented at CHT-04: An ICHMT International Symposium on Advances in Computational Heat Transfer, April 2004, G. de Vahl Davis and E. Leonardi (Eds.), CD-ROM Proceedings, ISBN 1-5670-174-2, Begell House, New York, 2004." In: *International Journal of Thermal Sciences* 45.1 (2006), pp. 70–85. ISSN: 1290-0729. DOI: https://doi.org/10.1016/j.ijthermalsci.2005.04.010. URL: https://www.sciencedirect.com/science/article/pii/S1290072905001341.

[14] *Evaluation of high temperature gas cooled reactor performance: Benchmark analysis related to initial testing of the HTTR and HTR-10*. IAEA-TECDOC-1382. International Atomic Energy Agency, 2013.

[15] Evaluated Nuclear Data File. *Fission cross-section for U235*. URL: https://www-nds.iaea.org/exfor/endf.htm. Accessed: 03.23.2023.

[16] Carlo Fiorina et al. "GeN-Foam: A novel OpenFOAM® based multi-physics solver for 2D/3D transient analysis of nuclear reactors". In: *Nuclear Engineering and Design* 294 (Dec. 2015), pp. 24–37. DOI: 10.1016/j.nucengdes.2015.05.035.

[17] *The Gemini Initiative*. URL: https://gemini-initiative.com/. (accessed: 10.10.2022).

[18] Generation IV International Forum. *Annular Report 2020*. URL: www.gen-4.org/gif/jcms/c_44720/annual-reports. (accessed: 03.19.2023).

[19] Michał Górkiewicz and Jerzy Cetnar. "Flattening of the Power Distribution in the HTGR Core with Structured Control Rods". In: *Energies* 14.21 (2021). ISSN: 1996-1073. DOI: 10.3390/en14217377. URL: https://www.mdpi.com/1996-1073/14/21/7377.

[20] *High-temperature Gas-cooled Reactors and Industrial Heat Applications*. NEA No. 7629. OECD, 2022.

[21] Alexander J. Huning, Sriram Chandrasekaran and Srinivas Garimella. "A review of recent advances in HTGR CFD and thermal fluid analysis". In: *Nuclear Engineering and Design* 373 (2021), p. 111013. ISSN: 0029-5493. DOI: https://doi.org/10.1016/j.nucengdes.2020.111013. URL: https://www.sciencedirect.com/science/article/pii/S0029549320305070.

[22] Serpent Wiki. *Multi-physics interface*. URL: https://serpent.vtt.fi/mediawiki/index.php/Multi-physics_interface. Accessed: 06.13.2023.

[23] Yoshitomo Inaba et al. “Evaluation of maximum fuel temperature in HTTR”. In: *Journal of Nuclear Science and Technology* 51.11-12 (2014), pp. 1336–1344. DOI: 10.1080/00223131.2014.941955. eprint: https://doi.org/10.1080/00223131.2014.941955. URL: https://doi.org/10.1080/00223131.2014.941955.

[24] *Outline of High Temperature Engineering Test Reactor*. URL: https://www.jaea.go.jp/04/o-arai/nhc/en/faq/httr.html. Accessed 03.19.2023.

[25] Japan Atomic Energy Agency. *Restart of High Temperature Engineering Test Reactor*. URL: https://www.jaea.go.jp/english/news/press/2021/073003/. Accessed: 05.16.2023.

[26] *Japan Atomic Energy Agency 2022 Business Report FY2021*. Annular Report. Japan Atomic Energy Agency, 2022.

[27] Min-Hwan Kim, Nam-il Tak and Jae-Man Noh. “Study on Influence of Turbulence Model Selection on Prediction of Flow Distribution and Hot Spot Fuel Temperature in Prismatic HTGR Cores”. In: *Engineering Applications of Computational Fluid Mechanics* 8.2 (2014), pp. 263–273. DOI: 10.1080/19942060.2014.11015512. eprint: https://doi.org/10.1080/19942060.2014.11015512. URL: https://doi.org/10.1080/19942060.2014.11015512.

[28] Zuzanna M. Krajewska et al. “Front-end investigations of the coated particles of nuclear fuel samples – ion polishing method”. In: *Nuclear Engineering and Technology* 54.6 (2022), pp. 1935–1946. ISSN: 1738-5733. DOI: https://doi.org/10.1016/j.net.2021.12.003. URL: https://www.sciencedirect.com/science/article/pii/S1738573321006720.

[29] Igor Królikowski and Jerzy Cetnar. “Neutronic and thermal-hydraulic coupling for 3D reactor core modeling combining MCB and fluent”. In: *Nukleonika* 60 (Sept. 2015). DOI: 10.1515/nuka-2015-0097.

[30] Jaakko Leppänen and M. Aufiero. “Development of an unstructured mesh based geometry model in the Serpent 2 Monte Carlo code”. English. In: *Proceedings of the international conference on physics of reactors*. Vol. JAEA-Conf 2014-003. Papers are in the zip file; International Conference on the Physics of Reactors, PHYSOR 2014 : The Role of Reactor Physics toward Sustainable Future, PHYSOR2014 ; Conference date: 28-09-2014 Through 03-10-2014. 2015.

[31] Jaakko Leppänen et al. “The Serpent Monte Carlo code: Status, development and applications in 2013”. In: *Annals of Nuclear Energy* 82 (2015). Joint International Conference on Supercomputing in Nuclear Applications and Monte

Carlo 2013, SNA + MC 2013. Pluri- and Trans-disciplinarity, Towards New Modeling and Numerical Simulation Paradigms, pp. 142–150. ISSN: 0306-4549. DOI: https://doi.org/10.1016/j.anucene.2014.08.024. URL: https://www.sciencedirect.com/science/article/pii/S0306454914004095.

[32] Jaakko Leppänen et al. "Unstructured mesh based multi-physics interface for CFD code coupling in the Serpent 2 Monte Carlo code". English. In: *Proceedings of the international conference on physics of reactors*. Vol. JAEA-Conf 2014-003. Papers in zip file; International Conference on the Physics of Reactors, PHYSOR 2014 : The Role of Reactor Physics toward Sustainable Future, PHYSOR2014 ; Conference date: 28-09-2014 Through 03-10-2014. 2015.

[33] Elmer E. Lewis. "Chapter 3 - Neutron Distributions in Energy". In: *Fundamentals of Nuclear Reactor Physics*. Ed. by Elmer E. Lewis. Burlington: Academic Press, 2008, pp. 57–84. ISBN: 978-0-12-370631-7. DOI: https://doi.org/10.1016/B978-0-12-370631-7.00003-6. URL: https://www.sciencedirect.com/science/article/pii/B9780123706317000036.

[34] Elmer E. Lewis. "Chapter 9 - Reactivity Feedback". In: *Fundamentals of Nuclear Reactor Physics*. Ed. by Elmer E. Lewis. Burlington: Academic Press, 2008, pp. 221–241. ISBN: 978-0-12-370631-7. DOI: https://doi.org/10.1016/B978-0-12-370631-7.00009-7. URL: https://www.sciencedirect.com/science/article/pii/B9780123706317000097.

[35] G. Longoni, RO. Gates and BK. Medowell. *High Temperature Gas Reactors: Assessment of Applicable Codes and Standards*. Pacific Northwest National Laboratory, 2015.

[36] ZHAO Lu et al. "A review of the coefficient of thermal expansion and thermal conductivity of graphite". In: *New Carbon Mater.* 37.20210191-SK-Review (2022), p. 544. ISSN: 2097-1605. DOI: 10.1016/S1872-5805(22)60603-6. URL: http://xxtcl.sxicc.ac.cn/en/article/doi/10.1016/S1872-5805(22)60603-6.

[37] NIST. *NIST Chemistry WebBook, SRD 69, helium.*

[38] W Pfeiffer, G Malek and K Lund. *POKE A Gas-Cooled Reactor Flow and Thermal Analysis Code*. GA-10226 Gulf Gen. At. Inc., 1970.

[39] M.M. Rahman et al. "Exploring SIMPLE algorithm for all speeds". In: *Ain Shams Engineering Journal* 14.2 (2023), p. 101854. ISSN: 2090-4479. DOI: https://doi.org/10.1016/j.asej.2022.101854. URL: https://www.sciencedirect.com/science/article/pii/S2090447922001654.

[40] *Review of Generation IV Nuclear Energy Systems*. Institut de Radioprotection et de Sûreté Nucléaire, 2015.

[41] P. Savva, M. Varvayanni and N. Catsaros. "Dependence of control rod worth on fuel burnup". In: *Nuclear Engineering and Design* 241.2 (2011), pp. 492–497. ISSN: 0029-5493. DOI: https://doi.org/10.1016/j.nucengdes.2010.11.021. URL: https://www.sciencedirect.com/science/article/pii/S0029549310007661.

[42] Taiju Shibata et al. "Present status of JAEA's RD toward HTGR deployment". In: *Nuclear Engineering and Design* 398 (2022), p. 111964. ISSN: 0029-5493. DOI: https://doi.org/10.1016/j.nucengdes.2022.111964. URL: https://www.sciencedirect.com/science/article/pii/S0029549322003156.

[43] SimScale GmbH. *K-Omega and K-Omega SST*. URL: https://www.simscale.com/docs/simulation-setup/global-settings/k-omega-sst/. Accessed: 05.31.2023.

[44] *Summary Review on the Application of Computational Fluid Dynamics in Nuclear Power Plant Design*. IAEA Nuclear Energy Series No. NR-T-1.20. International Atomic Energy Agency, 2022.

[45] Eiji Takada et al. "Core thermal–hydraulic design". In: *Nuclear Engineering and Design* 233.1 (2004). Japan's HTTR, pp. 37–43. ISSN: 0029-5493. DOI: https://doi.org/10.1016/j.nucengdes.2004.07.009. URL: https://www.sciencedirect.com/science/article/pii/S0029549304002365.

[46] Nobumasa Tsuji et al. "Study of the applicability of CFD calculation for HTTR reactor". In: *Nuclear Engineering and Design* 271 (2014). SI : HTR 2012, pp. 564–568. ISSN: 0029-5493. DOI: https://doi.org/10.1016/j.nucengdes.2013.12.033. URL: https://www.sciencedirect.com/science/article/pii/S0029549313007139.

[47] Riku Tuominen et al. "Coupling Serpent and OpenFOAM for neutronics - CFD multi-physics calculations". English. In: *PHYSOR 2016: Unifying Theory and Experiments in the 21st Century*. SDA: SHP: SASUNE Nuclear Project : 100502 ; International Conference on the Physics of Reactors, PHYSOR 2016 : Unifying Theory and Experiments in the 21st Century, PHYSOR 2016 ; Conference date: 01-05-2016 Through 05-05-2016. United States: American Nuclear Society (ANS), 2016, pp. 255–269. ISBN: 978-0-89448-762-2.

[48] *User Guide version 10*. The OpenFOAM Foundation, 2022.

[49] World Nuclear News. *China's demonstration HTR-PM reaches full power*. URL: https://www.world-nuclear-news.org/Articles/China-s-demonstration-HTR-PM-reaches-full-power. Accessed: 03.20.2023.

[50] Zuo-Yi Zhang et al. "600-MWe high-temperature gas-cooled reactor nuclear power plant HTR-PM600". In: *Nuclear Science and Techniques* 33.101 (2022). ISSN: 2210-3147. DOI: https://doi.org/10.1007/s41365-022-01089-9. URL: https://link.springer.com/article/10.1007/s41365-022-01089-9.